

Preindustrial to Present day Impact of Changes in Short-lived Pollutant Emissions  
on Atmospheric Composition and Climate Forcing

Vaishali Naik<sup>1\*</sup>, Larry W. Horowitz<sup>2</sup>, Arlene M. Fiore<sup>3</sup>, Paul Ginoux<sup>2</sup>, Jingqiu Mao<sup>4</sup>, A.  
Aghedo<sup>5,#</sup>, and Hiram Levy II<sup>2</sup>

<sup>1</sup> UCAR/NOAA Geophysical Fluid Dynamics Laboratory, Princeton, New Jersey.

<sup>2</sup> NOAA Geophysical Fluid Dynamics Laboratory, Princeton, New Jersey.

<sup>3</sup> Department of Earth and Environmental Sciences and Lamont-Doherty Earth-Observatory,  
Columbia University, Palisades, New York, New York.

<sup>4</sup> Atmospheric and Oceanic Sciences, Princeton University, Princeton, New Jersey.

<sup>5</sup> Jet Propulsion Laboratory, California Institute of Technology, Pasadena, California.

<sup>#</sup> Now at Civil and Environmental Engineering, Rice University, Houston, Texas.

**\*Corresponding Author:** Vaishali.Naik@noaa.gov

## Abstract

Reducing the abundance of short-lived climate forcing agents, including tropospheric ozone and aerosols, has been suggested as a near-term climate mitigation strategy. It is, therefore, useful to understand the historical impact these species have had on climate. We first evaluate the gas-phase chemistry simulated by the Geophysical Fluid Dynamics Laboratory atmospheric model (GFDL AM3), a chemistry-climate model, and then apply the model to examine the changes in atmospheric composition and the net climate forcing from preindustrial to present day changes in short-lived pollutant emissions using the new 1850-2000 emissions dataset of Lamarque et al. [2010]. Our base AM3 simulation driven with observed sea surface temperature and sea ice cover over the period 1981-2007, generally reproduces the observed mean magnitude, spatial distribution, and seasonal cycle of tropospheric ozone and carbon monoxide. To assess the impact of present day short-lived pollutant emissions relative to the preindustrial, we perform two additional simulations, both with fixed present-day climatological sea-surface temperature and sea-ice extent, present-day greenhouse gas and ozone depleting substance concentrations, but with preindustrial (1860) and present-day (2000) anthropogenic and biomass burning emissions of short-lived pollutants (the ozone precursors  $\text{NO}_x$ , CO and non-methane volatile organic compounds, and aerosols and their precursors). Comparing the two simulations, we find that the tropospheric ozone burden increases by 21% as a result of preindustrial to present emission changes, the global burden of sulfate aerosols increases by a factor of three, black carbon by a factor of 2.4 and organic carbon by 40% relative to preindustrial. We simulate a 10% increase in tropospheric hydroxyl concentration for present day relative to preindustrial, showing that increases in OH sources (ozone and nitrogen oxides) dominate over sinks (carbon monoxide, non-methane volatile organic compounds, and sulfur dioxide) in the absence of changes in

37 methane concentrations. Combined preindustrial to present-day changes in tropospheric ozone  
38 and aerosols cause a strong negative top-of-the-atmosphere forcing ( $-1.43 \text{ Wm}^{-2}$ ) indicating that  
39 the negative forcing (direct plus indirect) from aerosol changes dominates over the positive  
40 forcing due to ozone and black carbon increases, thus resulting in a net radiative cooling of the  
41 climate system.

42

## 1. Introduction

Although long-lived greenhouse gases in the atmosphere are the dominant contributors to climate change, short-lived climate forcing agents including tropospheric ozone, and sulfate and carbonaceous aerosols have also contributed considerably to the radiative forcing of climate since preindustrial times [Forster et al., 2007]. Controlling emissions of short-lived air pollutants with atmospheric lifetime of days to weeks has been suggested as a “fast-action” strategy for mitigating climate change [Hansen et al., 2000; Jackson, 2009; Molina et al., 2009; Penner et al., 2010; Shindell et al., 2012]. Several studies have demonstrated the importance of the future evolution of short-lived climate forcers on the climate system [Shindell et al., 2007, 2008; Levy et al., 2008; Menon et al., 2008; Liao et al., 2009]. Significant progress has been made in quantifying and reducing uncertainties in the preindustrial to present day radiative forcing due to individual short-lived climate forcers [Forster et al., 2007]. However, the net climate impact from preindustrial to present-day changes in short-lived pollutant emissions remains quite uncertain not only because of the uncertainties in their preindustrial emission estimates and atmospheric burden, but also because of the different ways they interact with radiation. For example, increases in tropospheric ozone contribute to climate warming, while the direct impact of increases in black carbon is a warming and that for increases in sulfate and organic carbon is a cooling of the Earth’s climate. Additionally, aerosols affect the radiation budget indirectly by interacting with clouds resulting in either a warming or cooling [Lohmann and Feichter, 2005; Forster et al., 2007; Mahowald et al., 2011]. Our goal here is to quantify the changes in atmospheric composition and the net climate forcing from preindustrial to present day changes in short-lived pollutant emissions only.

Short-lived pollutants interact in many ways to influence the atmospheric chemical composition and the Earth's radiation budget [Isaksen et al., 2009]. Changes in emissions of tropospheric ozone precursors, including nitrogen oxides ( $\text{NO}_x$ ), carbon monoxide ( $\text{CO}$ ) and non-methane volatile organic compounds (NMVOCs), influence the abundance of tropospheric ozone and its radiative forcing on climate. In addition, they affect the oxidizing capacity of the atmosphere, thereby influencing the lifetime of methane ( $\text{CH}_4$ ), a longer lived potent greenhouse gas and an ozone precursor [Fuglestvedt et al., 1999; Wild et al., 2001; Fiore et al., 2002; Naik et al., 2005; West et al., 2007]. Changes in the oxidizing capacity (driven by changes in ozone precursor emissions) can also impact the atmospheric burden of sulfate and nitrate aerosols as these are produced by the oxidation of precursor gases including sulfur dioxide ( $\text{SO}_2$ ),  $\text{NO}_x$ , and ammonia ( $\text{NH}_3$ ) [Unger et al., 2006]. Changes in aerosol burdens, either induced by chemistry or via direct controls on their emissions, impact heterogeneous chemistry, modify the atmospheric radiation budget and alter cloud properties, that can in turn affect ozone photochemistry [Martin et al., 2003; Bian et al., 2003; Lamarque et al., 2005a; Menon et al., 2008; Unger et al., 2009], and affect the hydrological cycle [Lohmann and Feichter 2005; Rosenfeld et al., 2008]. Furthermore, anthropogenic emissions of short-lived pollutants are strongly tied to economic development and modulated by air pollution controls. Heterogeneous emissions combined with non-linear chemical interactions result in strong spatial and temporal gradients of short-lived climate forcers, which cascades into an inhomogeneous, highly uncertain climate response.

In this study, we apply the Geophysical Fluid Dynamics Laboratory Atmospheric Model version 3 (GFDL AM3), a coupled chemistry-climate model, to investigate the changes in atmospheric composition and the impact on climate resulting from a change in the emissions of short-lived pollutants from preindustrial levels (year 1860) to present day (year 2000). In section

2, we describe the key features of the AM3 model and discuss the emissions and boundary conditions implemented in the model. We evaluate the results of a base simulation against observations in section 3. The impact of preindustrial to present-day short-lived pollutant emissions on atmospheric composition and climate forcing is presented in section 4. Finally, overall results are discussed and conclusions are reported in section 5.

## 2. Model Description

AM3 model, the atmospheric component of the GFDL coupled model (CM3) [Donner et al., 2011; Griffies et al., 2011], is developed from the GFDL AM2 [GFDL Global Atmospheric Model Development Team, 2004, hereafter GAMDT04] and has been applied recently to address key questions in chemistry-climate interactions [Fang et al., 2011; Rasmussen et al., 2011; Lin et al., 2012]. In addition to a number of significant dynamical and physical updates as described by Donner et al. [2011], the primary new feature of the model is that it simulates tropospheric and stratospheric chemistry interactively (with feedback to atmospheric radiation) over the full model domain. This unified representation of tropospheric and stratospheric chemistry in AM3 obviates prescribing the concentrations of chemical species important for calculating radiation balance as previously done [GAMDT04, Delworth et al., 2006], thereby removing inconsistencies between the model-generated meteorology and the atmospheric distributions of the forcing agents. The model uses a finite-volume dynamical core on a horizontal domain consisting of 6x48x48 cubed-sphere grid with the grid size varying from 163 km (at the 6 corners of the cubed sphere) to 231 km (near the center of each face), a resolution denoted as C48. The vertical domain of the model extends from the surface up to 0.01 hPa (86 km) with 48 vertical hybrid sigma pressure levels.

Chemical species undergo transport (advection, vertical diffusion and convection) in accordance with the AM3 model physics as described by Donner et al. [2011]. An additional key feature of the AM3 model physics is that it simulates aerosol-cloud interactions for liquid clouds [Ming and Ramaswamy, 2009; Golaz et al., 2011] that give rise to the “aerosol indirect effect” – aerosols act as cloud condensation nuclei (CCN) thus increasing cloud albedo (first indirect effect) and increasing cloud lifetime by suppressing precipitation (second indirect effect), and absorbing aerosols evaporate clouds counteracting the direct effect on radiation (semi-direct effect). Below we describe in detail the chemistry represented in AM3.

## **2.1. Chemistry**

Tropospheric trace gas chemistry in AM3 is based on a modified version of the chemical scheme used in the Model for OZone and Related Tracers version 2 (MOZART-2) [Horowitz et al., 2003, 2007]. It includes reactions of  $\text{NO}_x$ - $\text{HO}_x$ - $\text{O}_x$ - $\text{CO}$ - $\text{CH}_4$  and other NMVOCs. The oxidation of  $\text{SO}_2$  and dimethyl sulfide to form sulfate aerosol is fully coupled with the gas-phase chemistry. Organic carbonaceous aerosols are modeled as directly emitted primary organic aerosols (POA) and as secondary organic aerosols (SOA) formed by the oxidation of anthropogenic NMVOCs. We include seasonally-varying natural emissions of POA to represent the aerosols produced from the rapid oxidation of biogenic terpenes on the basis of work by Dentener et al. [2006]. In addition, we include a seasonally-varying SOA source of  $9.6 \text{ Tg yr}^{-1}$  from the oxidation of anthropogenic n-butane calculated offline from previous estimates of butane emissions and monthly OH fields following Tie et al. [2005]. Black carbon and primary organic carbon are converted from hydrophobic to hydrophilic state with e-folding times of 1.44 and 2.88 days, respectively [Donner et al., 2011]. Nitrate aerosols are simulated but do not impact

radiation calculations in this version of the model. Recent studies estimate that preindustrial to present day changes in nitrate aerosols have contributed only slightly to the aerosol forcing on climate, however, future reductions in sulfate precursors combined with increases in the emissions of ammonia may lead to a stronger role of nitrate aerosols in the climate system [Bauer et al., 2007; Bellouin, et al., 2011]. The size distribution of sea salt and mineral dust aerosols is represented by five size bins each, ranging from 0.1 to 10  $\mu\text{m}$  (dry radius). Representation of stratospheric chemistry is based on the formulation of Austin and Wilson [2010] that includes the important stratospheric  $\text{O}_3$  loss cycles ( $\text{O}_x$ ,  $\text{HO}_x$ ,  $\text{NO}_x$ ,  $\text{ClO}_x$ , and  $\text{BrO}_x$ ), and heterogeneous reactions on sulfate aerosols (liquid ternary solutions) and polar stratospheric clouds (nitric acid trihydrate (NAT) and water-ice). Heterogeneous reactions on liquid ternary solutions are represented based on Carslaw et al. (1994) and those on NAT polar stratospheric clouds are calculated as in Hanson and Mauresberger (1988). The rates of change of inorganic chlorine ( $\text{Cl}_y$ ) and inorganic bromine ( $\text{Br}_y$ ) are parameterized as a function of tropospheric concentrations of source gases (CFC11, CFC12,  $\text{CH}_3\text{Cl}$ ,  $\text{CCl}_4$ ,  $\text{CH}_3\text{CCl}_3$ , and HCFC22 for  $\text{Cl}_y$ , and  $\text{CH}_3\text{Br}$ , Halon1211 and Halon1301 for  $\text{Br}_y$ ) for computational efficiency to avoid transporting additional tracers in the model (discussed in detail in Austin et al., submitted). Changes in stratospheric ozone and water vapor feedback to the atmospheric radiation, thereby coupling the climate and chemistry.

The model simulates the atmospheric concentrations of 97 chemical species listed in Table 1 throughout the model domain, of which 16 are aerosol species that are discussed in detail elsewhere [Ginoux et al., in prep]. Here, we focus on the chemistry of 81 species (of which 62 transported) which undergo 183 gas-phase reactions and 41 photolytic reactions in the model. Kinetic reaction rates are based on JPL 2006 [Sander et al., 2006]. Clear-sky photolysis

frequencies are computed using a multivariate interpolation table resulting from calculations using the Tropospheric Ultraviolet and Visible radiation model version 4.4 [Madronich and Flocke, 1998]. Photolysis frequencies are adjusted for simulated overhead stratospheric ozone column, surface albedo, and clouds, but do not account for simulated aerosols. The chemical system is solved numerically using a fully implicit Euler backward method with Newton-Raphson iteration, as in Horowitz et al. [2003]. Changes in tropospheric ozone and aerosols feedback to atmospheric radiation.

## **2.2. Deposition**

Monthly mean dry-deposition velocities are included in the model for gaseous O<sub>3</sub>, CO, CH<sub>4</sub>, CH<sub>2</sub>O, CH<sub>3</sub>OOH, H<sub>2</sub>O<sub>2</sub>, NO<sub>2</sub>, HNO<sub>3</sub>, PAN, CH<sub>3</sub>COCH<sub>3</sub>, CH<sub>3</sub>COOOH, CH<sub>3</sub>CHO, CH<sub>3</sub>COCHO, NO and HNO<sub>4</sub>. Except for O<sub>3</sub> and PAN, the deposition velocities are calculated offline using a resistance-in-series scheme [Wesley, 1989; Hess et al., 2000] as described by Horowitz et al. [2003]. Dry deposition velocities for O<sub>3</sub> are taken from Bey et al. [2001] and those for PAN have been calculated interactively within MOZART version 4 with updates to the resistance-in-series scheme as described by Emmons et al. [2010]. A diurnal cycle is imposed on the monthly mean deposition velocity for O<sub>3</sub> as in Horowitz et al. [2003] Dry deposition of aerosols includes gravitational settling and impaction at the surface by turbulence.

Wet deposition of soluble gaseous species includes in-cloud and below-cloud scavenging by large-scale (ls) and convective clouds (cv) and are simulated as first-order loss processes. In-cloud scavenging of soluble gases (shown with an asterisk in Table 1) is calculated using the scheme of Giorgi and Chameides [1985]. Below cloud wet scavenging is only considered for

large-scale precipitation and is computed for gases following Henry's law as described in Brasseur et al. [1998]. The total rate of wet deposition (W) for a species is given by,

$$W = (\Gamma_{in}^{cv,ls} + \Gamma_{bc}^{ls}) \cdot C;$$

where, C is the local concentration of the gas,  $\Gamma_{in}^{cv,ls}$  ( $s^{-1}$ ) is the in-cloud scavenging coefficient for large-scale and convective precipitation, and  $\Gamma_{bc}^{ls}$  ( $s^{-1}$ ) is the below-cloud scavenging coefficient for large-scale precipitation. The in-cloud scavenging coefficient for soluble gases is,

$$\Gamma_{in}^{cv,ls} = 1 - e^{(-\beta \cdot f)}; \beta = \frac{P_{rain}^{k+1} - P_{rain}^k + P_{snow}^{k+1} - P_{snow}^k}{\Delta p \cdot g^{-1} \cdot \chi_{liq}},$$

where, f is the scavenging factor or the fraction of gas incorporated in cloud condensate and is determined by the Henry's law equilibrium [Donner et al., 2011],  $P^{k+1} - P^k$  is the precipitation flux generated in the layer k,  $\Delta p$  is the pressure thickness of the model layer k, g is the gravitational acceleration, and  $\chi_{liq}$  ( $= \frac{\text{cloud water (kg)}}{\text{air mass (kg)}}$ ) is the liquid water content calculated by the large-scale and convective cloud parameterizations. In-cloud wet removal for convective precipitation is computed only within the updraft plumes and mesoscale anvils. In-cloud scavenging is also considered for aerosols following the same scheme but with prescribed values of scavenging factor [Donner et al., 2011; Fang et al., 2011].

Below cloud scavenging of gases for large-scale precipitation is computed as

$$\Gamma_{bc}^{ls} = K_g (c_g - c_{g*}),$$

where,  $K_g = \frac{D_g}{d} \left[ 2 + 0.6 \sqrt{\left( \frac{dw_D}{v} \right)} \sqrt[3]{\left( \frac{v}{D_g} \right)} \right]$  is the gas-phase mass transfer coefficient,  $c_g$  and  $c_{g*}$  are the concentrations of the species in gas-phase and at the surface of the rain drop, respectively, the

diffusive coefficient  $D_g = 1.12 \times 10^{-5} \text{ m}^2 \text{ s}^{-1}$ , the mean diameter of rain drop  $d = 1.89 \times 10^{-3} \text{ m}$ , the rain drop terminal velocity  $w_D = 7.48 \text{ m s}^{-1}$  and the kinematic viscosity of air  $\nu = 6.18 \times 10^{-6} \text{ m}^2 \text{ s}^{-1}$ . Re-evaporation of falling precipitation (where  $P^{k+1} - P^k < 0$ ) returns dissolved species to the atmosphere as in Liu et al. [2001]. Below-cloud washout of aerosols for large-scale precipitation is parameterized as by Fang et al. [2011] and Li et al. [2008].

### 2.3. Emissions and Lower Boundary Conditions

Surface emissions of chemical species are from the new emissions dataset of Lamarque et al. [2010], developed for chemistry-climate model simulations for the Climate Model Inter-comparison Project Phase 5 (CMIP5) in support of the Intergovernmental Panel on Climate Change (IPCC) Fifth Assessment Report (AR5). The inventory provides monthly mean gridded emissions of reactive chemical species, including ozone precursors and aerosol species, at a horizontal resolution of  $0.5^\circ$  latitude  $\times$   $0.5^\circ$  longitude for each decade beginning 1850 to 2000. Emissions originating from anthropogenic sources (defined to include energy use in stationary and mobile sources, industrial processes, domestic and agricultural activities), open biomass burning (includes burning of grasslands and forests), ships and aircraft are provided. Surface anthropogenic emissions for the base year 2000 are generated by aggregating existing regional and global emission inventories for 40 world regions and 10 sectors (see Lamarque et al., 2010 for more details). Monthly emissions are given for all sources; however there is no seasonal variation in anthropogenic and ship emissions. Biomass burning emissions for the base year 2000 are from the GFED version 2 inventory [van der Werf et al., 2006]. No information on the vertical distribution of these emissions was provided in the original dataset. We distributed the biomass burning emissions over six ecosystem-dependent altitude regimes between the surface

and 6 km following the recommendations of Dentener et al. [2006]. Emissions from agricultural waste burning and fuelwood burning, which are usually specified with biomass burning, are included in anthropogenic residential sector emissions.

The inventory includes ship emissions from international and domestic shipping and fishing, which are based on a recent assessment by Eyring et al. [2009]. As noted by Lamarque et al. [2010], the spatial distribution of ship emissions does not account for dispersion, chemical transformation and sub-grid scale loss processes, which may lead to an over-estimate of ozone formation in global models. The inventory also includes aircraft emissions of nitrogen oxide and black carbon based on calculations using the FAST model [Lee et al., 2005] for the European Quantify project (<http://www.pa.op.dlr.de/quantify/>). Emissions are provided at altitude levels from about 0.3 km to 15 km. As aircraft SO<sub>2</sub> emissions are not provided in the inventory, we calculate these by scaling the aircraft emissions of BC by an emission ratio of 25 gSO<sub>2</sub>/g BC.

Estimates of emissions from natural sources, including plants, soils or oceans, are not provided by Lamarque et al. [2010]. We, therefore, use natural emissions for all relevant gaseous species, including isoprene, from the POET inventory (Precursors of Ozone and their Effects in the Troposphere) for 2000 [Granier et al., 2005] as implemented in MOZART-4 [Emmons et al. 2010]. Natural emissions vary from month-to-month, however they do not respond to changes in climate, vegetation or land-use. Soil emissions of NO<sub>x</sub> resulting from agricultural activities are included in anthropogenic sector in the emissions inventory of Lamarque et al. [2010]. Natural soil NO<sub>x</sub> emissions are set to preindustrial value of 3.6 Tg N yr<sup>-1</sup> as in Horowitz [2006]. Lightning NO<sub>x</sub> emissions in the model are calculated following Horowitz et al. [2003] as a function of subgrid convection parameterized in AM3 [Donner et al., 2011], resulting in a mean

1981-2000 total source of  $4.5 \pm 0.2$  Tg N (as NO) per year with diurnal, seasonal, and interannual variability based on the model meteorology.

Direct emissions of POA from biological activity in the ocean [O'Dowd et al. 2004] as a function of sea surface temperature and surface winds that vary with climate are also included. Dimethyl sulfide (DMS) emission is calculated using an empirical function of prescribed fixed monthly mean DMS concentration in sea water and wind speed at 10 m, as described by Chin et al. [2002]. Dust emissions are parameterized following Ginoux et al. [2001] and sea salt particles are emitted from the ocean according to Monahan et al. [1986].

Global total emissions for years 1860 and 2000 are presented in Table 2. Figure 1 shows the global distribution of the percent change in annual mean surface emissions of NO, CO, NMVOCs, black carbon, organic carbon, and SO<sub>2</sub>, from 1860 to 2000. Although, global mean short-lived pollutant emissions increase from preindustrial to present day (Table 2), emissions for some species from several regions of the world are lower in 2000 (Figure 1). For example, emissions of black carbon and organic carbon from the United States are lower in 2000 compared with 1860, driven by decreases in domestic fuel and biomass burning.

Globally uniform concentrations of well-mixed greenhouse gases (WMGGs), including, carbon dioxide (CO<sub>2</sub>), nitrous oxide (N<sub>2</sub>O), methane (CH<sub>4</sub>), and halocarbons (CFC-11, CFC-12, CFC-113, CCl<sub>4</sub>, CH<sub>3</sub>Cl, CH<sub>3</sub>CCl<sub>3</sub>, HCFC-22, Cl<sub>y</sub>, and Br<sub>y</sub>) are specified from the Representative Concentration Pathways database (<http://www.iiasa.ac.at/web-apps/tnt/RcpDb/>) developed for climate model simulations for CMIP5 in support of IPCC-AR5 [Meinshausen et al., 2011]. Global mean concentrations of CH<sub>4</sub> and N<sub>2</sub>O are specified at the surface as lower boundary conditions for chemistry.

## 2.4.Simulations

We perform a base simulation of AM3 for the period 1980-2007 forced with interannually varying observed sea surface temperatures (SSTs) and sea-ice cover (SIC) [Rayner et al. 2003], following the Atmospheric Model Intercomparison Project (AMIP) configuration. The simulation was run for 28 years with the first year for initial spin-up. We analyze results from this simulation in Section 3 to evaluate the capability of AM3 to simulate the chemical atmosphere.

We perform two additional simulations of AM3 to investigate the impact of changes in emissions of short-lived species from preindustrial to present levels. These simulations follow the configuration designed by the Atmospheric Chemistry and Climate Model Intercomparison Project (ACCMIP) [Shindell and Lamarque, 2011]. The “2000” simulation uses prescribed climatological monthly mean SSTs and SIC for the decade 1995-2004 taken from one ensemble member of the 5-member ensemble historical simulation of the GFDL coupled model (GFDL CM3) conducted according to the CMIP5 specifications in support of the IPCC-AR5 [John et al., 2012; Horowitz et al. in preparation]. Concentrations of WMGGs, including CH<sub>4</sub>, N<sub>2</sub>O, and ODSs, and emissions of short-lived pollutants (non-methane O<sub>3</sub> precursors and aerosols) are set to their year 2000 values. The “1860” simulation uses the same configuration, including the SST and SIC boundary conditions, and WMGG concentrations, except that short-lived pollutant emissions are set to their 1860 values as shown in Table 2. Because their natural emissions are constant, differences in O<sub>3</sub> precursor emissions between the two simulations come from only anthropogenic and biomass burning sources. Since emissions of dust, sea-salt, DMS and oceanic POA depend on climate variables, small differences in their emissions between the present-day and preindustrial (Table 1) simulations contribute to their burden changes. Both simulations were

run for 11 years with one year for spin-up to obtain a good signal to noise ratio. We compare results from these two simulations in Section 4 to assess the impact of preindustrial to present day changes in anthropogenic and biomass burning emissions of short-lived pollutants. While the configuration with prescribed climatological SST and SIC is computationally efficient as opposed to running the full coupled model, contrasting these simulations provides an estimate of only the fast atmospheric responses but not the slow feedbacks that involve ocean surface temperature changes [Haywood et al., 2009].

### 3. Model Evaluation

We analyze mean results for the 1981-2000 time period from our base simulation, unless noted otherwise. The climate and dynamics simulated in this model integration have been evaluated in detail by Donner et al. [2011]. The general features of simulated stratospheric ozone have been evaluated by Donner et al. [2011] and Austin et al. [submitted to J. Climate]. Aerosols are evaluated by Ginoux et al. [in prep]. Here, we evaluate the gas-phase chemistry in the model through comparisons of simulated tropospheric ozone and CO with observations.

#### 3.1. Ozone

An annual global tropospheric (defined as the domain for which  $O_3$  concentration is less than 150 ppbv)  $O_3$  burden of 360 Tg is simulated by AM3 (Table 3). The photochemical production and destruction of  $O_3$  are simulated to be  $5753 \text{ Tg yr}^{-1}$  and  $5019 \text{ Tg yr}^{-1}$ , respectively. Net photochemical production of  $734 \text{ Tg yr}^{-1}$  in the troposphere exceeds the stratospheric influx (diagnosed in AM3 as the net dynamical flux) of  $450 \text{ Tg yr}^{-1}$ . Tropospheric loss by dry deposition at the surface accounts for  $1205 \text{ Tg yr}^{-1}$ . The simulated tropospheric  $O_3$  lifetime,

calculated as the ratio of O<sub>3</sub> burden and the total loss rate (photochemical loss plus surface deposition) is 21.1 days. Our simulated tropospheric O<sub>3</sub> burden is within 10% of  $335 \pm 10$  Tg derived from observation-based O<sub>3</sub> climatology [Wild, 2007]. A recent multi-model inter-comparison study of ozone and its precursors estimates the mean tropospheric O<sub>3</sub> production and loss to be  $5110 \pm 606$  Tg yr<sup>-1</sup> and  $4668 \pm 727$  Tg yr<sup>-1</sup> for present day conditions (year 2000), where the range is the multi-model standard deviation [Stevenson et al., 2006]. The multi-model mean dry deposition is  $1003 \pm 200$  Tg yr<sup>-1</sup>, the stratospheric influx inferred from the models as the residual of all other budget terms is  $552 \pm 168$  Tg yr<sup>-1</sup> and the mean tropospheric O<sub>3</sub> lifetime is 22.3 days. The AM3 tropospheric O<sub>3</sub> budget terms are well within the range of these numbers, with the O<sub>3</sub> production, loss and dry deposition at the high end, while AM3 stratospheric flux is at the lower end of the multi-model mean.

We evaluate the simulated seasonal cycle of ozone in the lower stratosphere and troposphere by comparison with ozonesonde measurements made between 1995 and 2009. The observations are taken from the climatology described by Tilmes et al. [2011] built on previous work by Logan et al. [1999]. Since the observed data is for 1995-2009, we compare the base simulation averaged over both 1981-2000 and 1995-2007 time periods (Figure 2). With the exception of a few sites, AM3 simulated ozone concentrations are within 10-15 ppbv of the observed values and reproduce the observed seasonal cycle, consistent with results from other chemistry-climate models [Shindell et al., 2006; Lamarque et al., 2012]. We also find that overall the comparison of AM3 O<sub>3</sub> averaged over 1995-2007 is very similar to that with O<sub>3</sub> averaged over the baseline time period of 1981-2000. At northern high latitude sites (Alert and Resolute), AM3 reproduces well the timing of the spring maximum in the lower troposphere and the late spring maximum in the middle troposphere but the magnitude of the simulated O<sub>3</sub> concentrations

is biased high compared with observations. In the upper troposphere, AM3 simulates a weaker seasonal variability compared with observations and underestimates the observed  $O_3$  concentrations by about 10-12%. This low bias at 200 mb is consistent with the underestimate of lower stratospheric ozone at northern high latitudes attributed to a deficiency in model transport (Figure 7 in [Donner et al., 2011]).

The seasonal variability in ozone observed at northern middle latitude stations (Hohenpeissenberg and Wallops Island) is captured by AM3, particularly in the lower and upper troposphere. The timing of peak ozone in AM3 is consistent with observations (spring in the upper troposphere transitioning to summer in the lower troposphere). A weaker seasonal cycle, however, is simulated in the mid troposphere in this region. At Southern Hemisphere tropical (Samoa) and mid-latitude (Lauder) stations, AM3 overestimates the observed  $O_3$  concentrations throughout the troposphere, except for Samoa at 500 mb where the AM3 slightly underestimates the observations. The shape of the seasonal cycle is well reproduced for the middle latitude site; however, for the tropical station, AM3 simulates peak  $O_3$  a few months earlier than that observed for the three levels shown in Figure 2.

We also compare the AM3 model zonal mean distribution of tropospheric  $O_3$  concentrations with those measured by the Tropospheric Emission Spectrometer (TES) instrument aboard the NASA-Aura satellite for the period 2005 to 2007 (Figure 3a). After interpolating the monthly mean AM3 ozone fields for 2005-2007 to TES pressure levels and applying the TES averaging kernels and a priori matrix to account for differences in vertical resolution and the influence of clouds [Kulawik et al., 2006], we find that AM3 is within  $\pm 20$  ppb (0-5%) from surface to mid-troposphere compared with TES observations (Figure 3a), consistent with the comparison of AM3 with ozonesonde data discussed above. Comparison of

model with TES in the upper troposphere/lower stratosphere at high latitudes is not meaningful as the sensitivity of TES is low in that region [Nassar et al., 2008]. Aghedo et al. [2011] show that applying the monthly mean TES averaging kernels (AKs) and a priori profiles to monthly mean model O<sub>3</sub> produces negligible biases compared to convolving the simulated O<sub>3</sub> with TES AKs each day at the overpass time. The bias of AM3 with respect to TES cannot be explained by the 3 – 10 ppbv positive biases showed when TES ozone measured in October 2004 to October 2006 were evaluated against ozonesondes [Nassar et al., 2008]. The full diagnoses of the cause of the AM3 model biases would be outside the scope of this paper, because it may be due to a combination of transport, emission and chemistry errors.

We also evaluated the AM3 simulated surface O<sub>3</sub> concentrations by comparison with data from surface observational networks in the United States (Clean Air Status and Trends Network – CASTNet <http://www.epa.gov/castnet/>), Europe (European Monitoring and Evaluation Programme – EMEP <http://www.nilu.no/projects/ccc/emepdata.html>), and published data from a few rural sites in India as shown in the supplementary information. We find that AM3 is able to reproduce the observed concentrations and seasonal cycles at two out of six regions in both the United States and Europe, and two out of three sites in India. While AM3 captures the seasonal cycle in most of the other regions, annual mean biases range from 8 to 20 ppb.

### **3.2. Carbon Monoxide**

We evaluate AM3 simulated CO mixing ratios near the surface against observed climatologies for 18 selected stations in the National Oceanic and Atmospheric Administration Environmental Science and Research Laboratory (NOAA ESRL) Carbon Cycle Cooperative

Global Air Sampling Network [Novelli and Masarie, 2010]. Monthly mean data over the period 1988-2009 has been used to create a climatology for each station. AM3 is sampled at the gridbox and altitude level corresponding to each station (Figure 4). In general, higher CO concentrations are observed in the northern hemisphere than in the southern hemisphere because of higher source strength in the northern hemisphere. The seasonal cycle at high and mid-latitudes in the northern hemisphere is strongly a function of photochemistry, with reduced OH abundance and weak vertical mixing resulting in accumulation of CO in the wintertime and increased OH leading to a significant decline in CO concentrations in summer. Peak CO concentrations at northern high and mid-latitudes are observed in spring while the minimum is at the end of summer. AM3 underestimates the seasonal variation in CO at all the northern high and mid latitude sites considered here (Figures 4a-f). The discrepancy is largest in late winter and spring when AM3 is biased low by 30-50 ppbv compared with the observations, similar to the multi-model biases discussed in Shindell et al [2006a]. The negative biases could stem from high OH concentrations (see section 3.3 for a discussion of OH), the neglect of any seasonality in anthropogenic CO emissions [Shindell et al., 2006a], or an underestimate of the total source of CO (direct and indirect from VOCs) in AM3.

Observations show lower CO concentrations in the tropics than those at northern high and mid-latitudes because of lower emissions and more rapid loss. In the tropics, the observed seasonality is governed by both anthropogenic and biomass burning emissions, with biomass burning emissions more important close to the equator and in the southern hemisphere tropics [Novelli et al. 1998 Duncan et al., 2007]. AM3 underestimates the seasonality and the magnitude of CO observed at most sites in the northern tropics (Figures 4h-4k). The observed spring time peak CO at Mauna Loa and Mariana Islands is attributed primarily to transport of pollution from

Asia [Brasseur et al., 1996; Jaffe et al., 1997]. AM3 does not capture the springtime peak at these stations indicating a possible problem with model transport and/or the magnitude of anthropogenic emissions from Asia. Mariana Islands is also influenced by dry season (spring) biomass burning in Southeast Asia [Jaffe et al., 1997], where springtime CO concentrations in AM3 are lower than those observed, suggesting a problem with our biomass burning emissions. AM3 reproduces the observed spring maximum at Christmas Island but simulates a second peak in fall indicating a problem in the timing of biomass burning emissions. Weakness in the seasonal cycle of biomass burning emissions in AM3 is further highlighted by the early peak (by three months) in simulated CO compared with observations at Ascension Island, a site most sensitive to biomass burning in southern Africa [Novelli et al., 1998]. AM3 captures fairly well the seasonal cycle at subtropical sites in the Southern Hemisphere (Tutuila, Easter Island) sites, but is biased low. In the southern high and mid latitudes where CO concentrations are generally lower and the seasonality is determined by a combination of biomass burning emissions, oceanic emissions, and in-situ hydrocarbon oxidation [Holloway et al. 2000], AM3 does an excellent job of reproducing the observed magnitude and seasonal variation of CO.

We also compare zonal mean AM3 tropospheric CO concentrations for 2005-2007 with those observed by TES (Figure 3b), after interpolating to TES pressure levels and applying the TES averaging kernels and a priori matrix. The patterns of global TES CO distributions in the troposphere have been found to agree with those from other satellites (e.g. MOPITT; [Luo et al., 2007a; Ho et al., 2009]). TES CO profiles are also found to be within 10% of averaged in-situ measurements [Luo et al., 2007b; Lopez et al., 2008]. AM3 underestimates the TES CO abundance by 20 ppbv in the northern extra-tropics throughout the troposphere and by 5-10 ppb in the southern troposphere, consistent with the comparison with surface CO measurements. TES

provides little information at the poles hence the comparison is not meaningful in that region  
[Luo et al., 2007a, Richards et al., 2006]

### 3.3. Hydroxyl radical and Methane lifetime

Hydroxyl radical (OH) determines the oxidizing capacity of the atmosphere, influencing the lifetime of many short-lived gaseous species [Levy 1971]. The tropospheric OH concentration strongly depends on the atmospheric abundance of O<sub>3</sub>, NO<sub>x</sub>, CO, hydrocarbons, water vapor and the distribution of solar radiation. Primary production of OH occurs when electronically excited O(<sup>1</sup>D), produced by the photolysis of O<sub>3</sub>, combines with water molecules [Levy 1971, Logan et al., 1981, Spivakovsky et al., 2000]. Therefore, OH concentrations are highest in the tropical lower to middle troposphere reflecting high levels of water vapor and ultraviolet radiation. Reaction with CO, CH<sub>4</sub> and NMVOCs, the dominant loss process of OH, produces hydro peroxy radical (HO<sub>2</sub>) that can regenerate OH via its reaction with NO and O<sub>3</sub> [Crutzen, 1973]. This secondary production of OH via radical recycling by NO<sub>x</sub> plays a more important role at higher latitudes where O(<sup>1</sup>D) and water vapor are less abundant [Spivakovsky et al., 2000, Lelieveld, 2002].

AM3 simulates a global mean airmass-weighted OH concentration of  $1.05 \pm 0.02 \times 10^6$  molecules cm<sup>-3</sup> for the 1981-2000 period, with a northern to southern hemisphere (NH/SH) ratio of 1.16 suggesting that higher concentrations of O<sub>3</sub>, NO<sub>x</sub> and other OH precursors in the northern hemisphere dominate over the higher concentrations of CO, VOCs, and other sinks for OH in the model. While observational constraints on OH (more discussed below) indicate that the annual mean OH concentration is higher in the southern hemisphere than the northern hemisphere

(NH/SH < 1) [Prinn et al., 2001; Montzka et al., 2000; Krol and Lelieveld, 2003], most chemistry models [Wang et al., 1998; Dalsøren and Isaksen, 2006], including AM3, simulate higher northern hemisphere OH concentrations (NH/SH > 1). Krol and Lelieveld [2003] suggest that this discrepancy arises because the location of the Intertropical Convergence Zone (ITCZ) is used to determine the interhemispheric ratio from observations, while models assume that the hemispheres are symmetric around the equator. However, the ITCZ is used only in the analysis of Montzka et al. [2000], while Prinn et al. [2001] divides the hemispheres at the equator. A possible reason for the AM3 overestimate of OH in the northern hemisphere could be the underestimate of northern hemisphere CO (Section 3.2).

We compare the AM3 simulated airmass-weighted annual mean OH concentrations (Figure 5a) with the climatology of Spivakovsky et al. [2000] (Figure 5b) for twelve tropospheric subdomains as recommended by Lawrence et al. [2001]. Mean AM3 simulates the highest boundary layer (surface to 750 hPa) OH burden in the tropics followed by the northern extra-tropics (30°N-90°N) and the southern extra-tropics (30°S-90°S), consistent with the climatology (Figure 5b), but is higher by about 25-35%. AM3 OH concentrations in the tropics decrease with increasing altitude as opposed to first decreasing in the mid-troposphere and then increasing in the upper troposphere as in the Spivakovsky et al [2000] climatology. Excessive OH in the tropical boundary layer could indicate limitations in our treatment of higher volatile organic compounds. For example, AM3 does not include representation of higher (5 and more carbon atoms) alkanes, alkenes and aromatic compounds, thus, reducing the OH sink (for example, the MOZART-4 mechanism which includes higher NMVOC yields an OH vertical distribution that better matches the climatology [Emmons et al., 2010]).

Simulated global mean tropospheric OH concentrations can be tested against indirect estimates from observationally constrained budgets of species with known sources and reaction with OH as their primary sink, such as 1, 1, 1-trichloroethane ( $\text{CH}_3\text{CCl}_3$ , methyl chloroform),  $^{14}\text{CO}$ , and  $\text{CHClF}_2$  (HCFC-22) [Spivakovsky et al., 2000 and references therein]. The lifetime of  $\text{CH}_3\text{CCl}_3$  derived from its observed atmospheric abundances and known industrial emissions has most often been used to estimate the global mean abundance of OH [Prinn et al., 1995, 2001; Krol et al., 1998; Krol and Lelieveld, 2003; Montzka et al., 2000, 2011]. Prinn et al [2001] estimated a global tropospheric mean  $\text{CH}_3\text{CCl}_3$  lifetime of  $5.99^{+0.95}_{-0.71}$  for the period 1978-2000. Since AM3 does not simulate the chemistry of  $\text{CH}_3\text{CCl}_3$ , we assume a global uniform atmospheric mixing ratio to calculate its tropospheric lifetime as,  $\tau_{\text{OH}} = \frac{1}{\int_{\text{sfc}}^{\text{trop}} k(T)[\text{OH}]}$ , where,  $k(T)$ , the rate constant for the oxidation of  $\text{CH}_3\text{CCl}_3$  by tropospheric OH, is  $1.64 \times 10^{-12} \exp(-1520/T) \text{ molec}^{-1} \text{ cm}^3 \text{ s}^{-1}$  [Sander et al., 2006]. Our estimated  $\text{CH}_3\text{CCl}_3$  tropospheric mean lifetime of  $5.3 \pm 0.1$  years over the period 1981-2000 is about 11% lower than the mean observation-derived lifetime estimate of Prinn et al. [2001]; while within the uncertainty range, we conclude that AM3 OH is likely biased high.

AM3 simulates a mean total atmospheric methane burden of 4622 Tg and tropospheric methane loss by reaction with OH of  $540 \text{ Tg yr}^{-1}$ , resulting in mean tropospheric methane lifetime against loss by tropospheric OH of 8.6 yr, about 10% lower than the lifetime of 9.6 years reported by Prather et al. [2001]. It is within the range of values (7.8-10.5 years) simulated by other models [Lawrence et al., 2001; Folberth et al., 2006; Jöckel et al. 2006; Fiore et al., 2009; Emmons et al., 2010]. Including a nominal stratospheric sink of  $40 \text{ Tg yr}^{-1}$  and a soil sink of  $30 \text{ Tg yr}^{-1}$ , yields a global atmospheric  $\text{CH}_4$  lifetime of 7.6 yr, on the low side of the  $8.7 \pm 1.3$  years range from a multi-model estimate [Stevenson et al. 2006].

492

## 493 **4. Impact of Short-lived pollutants on Composition and Climate**

494         We compare 10-year annual mean fields from 2000 and 1860 simulations to investigate  
495 the impact of changes in short-lived pollutant emissions from preindustrial to present levels, on  
496 atmospheric composition and climate below.

### 497 **4.1. Impact on Atmospheric Composition**

498         The impact of changes in short-lived pollutant emissions from 1860 to 2000 on global  
499 mean budget and burdens is shown in Table 3. We simulate a 21% increase in the annual mean  
500 global tropospheric O<sub>3</sub> burden from 302 Tg in preindustrial to 365 Tg in the present day. The  
501 photochemical production and loss of ozone increase by 45% and 40%, respectively. The  
502 deposition flux of ozone increases by ~50% in response to the increased ozone burden. The  
503 (photochemical and depositional) lifetime of ozone decreases from 25 days in the preindustrial to  
504 21 days in the present day simulation. In addition, the cross-tropopause flux of ozone increases  
505 by about 10% in the present day relative to the preindustrial simulation possibly because of a  
506 dynamical response resulting in a slight shift of the tropopause. Since we set CH<sub>4</sub> to its 2000  
507 level in both the 1860 and 2000 simulations, this preindustrial to present day increase in O<sub>3</sub>  
508 burden is on the lower side of that published in the literature [Lamarque et al., 2005b and  
509 references therein]. Indeed, Wang and Jacob [1998] show that using present-day CH<sub>4</sub>  
510 concentrations in preindustrial simulations decreases their estimated preindustrial to present day  
511 tropospheric O<sub>3</sub> burden enhancement from 63% to 44%. Our simulated increases in ozone  
512 photochemical production, loss and dry deposition are significantly lower than the estimates of  
513 Wang and Jacob [1998].

Of the total 64 Tg increase in tropospheric O<sub>3</sub> burden, 71% occurs in the northern hemisphere, consistent with the much larger NO<sub>x</sub> emission increase in the northern hemisphere. Global total column O<sub>3</sub> increases by about 3% with more than two-thirds of this increase occurring in the troposphere. Note that ozone depleting substances in the 1860 simulations are held at the present-day value, so our preindustrial to present day change does not include ODS-driven anthropogenic ozone depletion in the stratosphere. Total annual column O<sub>3</sub> increases of 20 to 30 DU are simulated over the industrialized areas of the northern hemisphere (Figure 6a). Global annual average surface O<sub>3</sub> concentrations increase by 10 ppbv from preindustrial to present-day, with largest increases simulated over regions of largest precursor emission increases (Figure 6b). The inter-hemispheric asymmetry in surface O<sub>3</sub> concentrations increases from NH/SH = 1.09 in preindustrial to NH/SH = 1.40 at present day owing to the large increases in short-lived O<sub>3</sub> precursor emissions, particularly NO<sub>x</sub>, in the northern hemisphere.

The global total annual burden of CO increases by 30% from preindustrial to present day. Changes in CO sources are only due to changes in the anthropogenic and biomass burning emissions of CO and NMVOC, hence they are somewhat lower than those expected if CH<sub>4</sub> were set to its preindustrial level in the 1860 simulation. Near-homogenous increases in CO burden are simulated (Figure 6c), except for strong source regions, for example, the biomass burning areas of Southeast Asia, Central Africa, and anthropogenic emissions areas of North America, China and South Asia. Increases in zonal average CO concentrations extend from the surface to the tropopause, with increases of 30 to 60 ppb in the northern hemisphere and 10 to 20 ppb in the southern hemisphere (not shown). Surface CO concentration increases of up to 400 ppb are simulated locally over source regions (Figure 6d). Reductions of about 10 ppb are simulated

locally for a few regions where biomass burning decreases (Figure 1) and is the primary source of CO.

The annual mean tropospheric NO<sub>x</sub> burden increases by 40% in the present day relative to preindustrial. NO<sub>x</sub> emissions from lightning, the main source of NO<sub>x</sub> in the free troposphere, particularly in preindustrial, decrease in the present day (Table 3). Reduced convective activity (not shown) in response to changes in short-lived pollutant emissions from preindustrial to present day decreases lightning NO<sub>x</sub> emissions. Strong tropospheric NO<sub>x</sub> burden increases are simulated near source regions particularly in the northern hemisphere (Figure 6e). Annual mean surface NO<sub>x</sub> concentrations increase by up to 3 ppbv over the northeastern US, Europe, northern India and China source regions, following the preindustrial to present day increases in emissions (Figure 1). Surface NO<sub>x</sub> increases are also simulated above ship track areas over the oceans. With a lifetime of a day, most NO<sub>x</sub> increases occur closer to the surface as opposed to the CO increases that are more homogenous throughout the troposphere.

Simulated global total burden of sulfate increases by a factor of three from preindustrial to present day (Table 3), within the range of previous estimates [Horowitz, 2006; Tsigaridis et al., 2006]. Largest increases are in the 0 to 30°N latitude band characterized by high emissions and oxidation capacity (Figure 6g). The burden of sulfate aerosols in the atmosphere depends on its sources (SO<sub>2</sub> emissions, level of atmospheric oxidants, including O<sub>3</sub>, OH, NO<sub>3</sub><sup>-</sup> and H<sub>2</sub>O<sub>2</sub>) and its sinks (wet and dry deposition). Higher present day versus preindustrial SO<sub>2</sub> emissions lead to increased formation of sulfate aerosols in the present day simulation. At the surface, sulfate concentrations increase up to 15 μg m<sup>-3</sup> in regions of high SO<sub>2</sub> emissions (Asia, Europe, and North America). Secondary maxima in the increase of surface sulfate concentrations occur in the

southern hemisphere over regions of high biomass burning (South America, Africa, and Southeast Asia).

The global total burden of carbonaceous aerosols increases from preindustrial to present day with BC aerosols increasing by a factor of 2.4 and organic carbon increasing by a smaller fraction (40%) because of larger background natural sources. The atmospheric burden of carbonaceous aerosols is governed by their emissions and deposition (wet and dry). BC emissions are driven by human activities that involve combustion of mostly fossil fuels with smaller contributions from domestic biofuel burning and biomass burning, whereas OC emissions predominantly come from the latter two categories. Reduced present-day emissions from domestic biofuel burning and forest clearing in the mid-latitude regions (North America, Europe, and Australia) drive decreases in carbonaceous aerosol burden over these regions (Figures 6i,k). On the other hand, sharp increases are simulated for regions with high present day emissions (China, India, central Africa). Changes in the burden are dominated by changes near the surface. Simulated surface concentrations in the present-day are lower over most of North America, Europe, and Australia, and increase in highly populated areas of Asia, Eastern Europe and central Africa (Figures 6k,l).

Next, we investigate the changes in the tropospheric oxidizing capacity from preindustrial to present day changes in short-lived pollutant emissions. Despite only minor changes in water vapor and reduced ultraviolet tropospheric O<sub>3</sub> photolysis rates (not shown), tropospheric mean air-mass-weighted OH concentrations increase by 10% from preindustrial to present day, acting to reduce the tropospheric lifetime of methane by 14%. Comparison of OH in various subdomains of the atmosphere indicates OH increases in all parts of the atmosphere except in the upper troposphere of the southern hemisphere, with the largest increases (30-60%) occurring in

the lower troposphere of the northern hemisphere (Figure 5c), coincident with the largest increases in  $\text{NO}_x$  and  $\text{O}_3$ . The almost symmetric OH concentrations across the equator in our preindustrial simulation (NH/SH ratio of 1.05) become asymmetric in the present-day (NH/SH ratio of 1.2), implying a dominant role for  $\text{NO}_x$  emissions. Figure 5d shows the spatial distribution of the increase in OH in the lowest atmospheric subdomain (surface to 750 hPa) where more than 60% of the total oxidation of methane occurs [Lawrence et al., 2001]. Almost a factor of two increase in OH is simulated over regions with high present day emissions of  $\text{NO}_x$ , CO and NMVOCs, mostly in the northern hemisphere.

An enhancement of OH largely indicates the dominance of increases in  $\text{O}_3$  and  $\text{NO}_x$  (source of OH) over increases in CO, NMVOCs, and  $\text{SO}_2$  (sinks of OH). Previous modeling studies of changes in tropospheric mean OH abundance from preindustrial to present day range from increases of 6-15% [Crutzen and Bruhl, 1993; Martinerie et al., 1995; Berntsen et al., 1997] to decreases of 5-33% [Thompson et al., 1992; Wang and Jacob, 1998; Mickley et al., 1999; Hauglustaine and Brasseur, 2001; Grenfell et al., 2001; Lelieveld et al., 2002; Shindell et al., 2003; Wong et al., 2004; Lamarque et al., 2005b; Shindell et al., 2006b; Skeie et al., 2010; Sofen et al., 2011; John et al., 2012]. Although our estimate of the preindustrial to present-day change in OH concentrations falls within the range of these studies, it is not directly comparable because we keep  $\text{CH}_4$  at its present day (2000) levels in both the simulations (among other model differences), yielding a larger preindustrial to present day OH increase.  $\text{CH}_4$  (and CO) are the main sink for OH in the background troposphere. Our preindustrial simulation is characterized by a lower than actual OH abundance because of enhanced OH loss in a low- $\text{NO}_x$  and high  $\text{CH}_4$  environment. Comparing their present-day with a sensitivity simulation of preindustrial atmosphere with present-day  $\text{CH}_4$  concentrations, Wang and Jacob [1998] estimate

a 9.5% increase in mean tropospheric mass-weighted OH concentration, consistent with our simulated 10% increase in OH.

## **4.2. Impact on Climate**

To investigate the impact of changes in short-lived pollutant emissions from preindustrial to present-day on climate, we first assess the net adjusted radiative forcing from these emission changes and then briefly explore the changes in key climate variables. Note that we expect the climate responses to be weak since our experiments are conducted with fixed SST and SIC. Radiative fluxes simulated in the two runs allow us to diagnose the radiative forcing as the change in the net irradiance (solar plus longwave radiation) at the top of the atmosphere (TOA) for the present day relative to the preindustrial simulation. Since our present day and preindustrial simulations use fixed SST and SIC extent, our calculated TOA radiative forcing, more appropriately referred to as “radiative flux perturbation” (RFP), incorporates the effects of fast atmospheric responses to short-lived pollutants but not the slow feedbacks associated with changes in global ocean temperatures [Hansen et al., 2005; Forster et al., 2007; Haywood et al., 2009]. RFP at the TOA has been shown to predict the global mean surface temperature change that will result from changes in short-lived pollutants [Hansen et al., 2005; Forster et al., 2007; Lohmann et al., 2010]. We do not diagnose the contribution of individual short-lived climate forcers to the net RFP.

The net global mean annual average all-sky TOA RFP due to short-lived pollutant emissions at present day relative to preindustrial is  $-1.43 \text{ Wm}^{-2}$  in our model, implying a net radiative cooling of the climate system. Tropospheric ozone increases produce a positive forcing

while aerosol increases exert either a positive forcing (black carbon) or a negative forcing (sulfate, organic carbon) on the climate system. Aerosols also produce a negative forcing indirectly via changes in cloud optical properties or a positive forcing from changes in the thermal structure of the atmosphere. Our results indicate that the strong negative forcing (direct plus indirect) from preindustrial to present day aerosol changes dominates over the positive forcing due to O<sub>3</sub> increases and aerosol semi-direct effect.

Figure 7a shows the geographical distribution of the annual mean all-sky TOA RFP due to preindustrial to present day short-lived pollutant emissions. The largest statistically significant negative RFPs (up to -10 Wm<sup>-2</sup>) are simulated over industrialized regions of northern hemisphere characterized by high aerosol burdens (China, India, Europe, North America). Smaller negative RFPs are also simulated for regions where biomass burning emissions increased over the last century, such as, south-east Asia, central Africa, and the Amazon, and over oceans downwind of source regions. Small positive RFP is simulated over much of the southern hemisphere oceans, the Arctic and parts of Australia. The simulated positive forcing in these regions is statistically insignificant relative to the model internal variability, possibly because 10 year runs are too short to produce a robust signal that can be distinguished from noise [Golaz et al., 2011].

To explore the role of changes in cloud properties on radiative forcing, we breakdown the all-sky RFP to clear-sky and cloudy-sky components. Clear-sky radiative fluxes are computed within the model by calling the radiation code in the absence of clouds for diagnostic purposes, so they do not include the impact of aerosol indirect effects and also do not include cloud modifications of direct effect through masking [Golaz et al., 2011]. We calculate the cloudy-sky RFP by taking the difference between all- and clear-sky RFP. Figures 7b and 7c show the spatial distribution of the clear-sky and cloudy-sky RFPs. From a global mean perspective, both the

clear and cloudy sky RFP are negative and the contribution of clear-sky RFP ( $-0.76 \text{ Wm}^{-2}$ ) to the all-sky RFP is only slightly higher than that of the cloudy sky RFP ( $-0.67 \text{ Wm}^{-2}$ ). Spatially, negative RFPs over and downwind of industrialized areas in the northern hemisphere, biomass burning regions, and neighboring oceans persist in the clear-sky component (Figure 7b), suggesting the dominance of reflecting aerosols (sulfate and organic) over absorbing aerosols (black carbon) and tropospheric ozone. The spatial pattern of cloudy-sky RFP resembles (global mean pattern correlation coefficient of  $-0.63$ ) that of the change in cloud liquid water path (LWP) (see supplementary Figure S2d). Regions with increasing LWP are associated with negative RF, for example, north-east US, China, and India, while regions with decreasing LWP are associated with positive RF, for example, over south-central Africa.

Next, we analyze the change in net radiative fluxes at the surface as changes in the surface radiation budget influence the hydrological cycle. Preindustrial to present-day change in short-lived pollutant emissions results in a global mean all-sky surface RFP of  $-2.6 \text{ Wm}^{-2}$ , implying that the emission changes result in an additional  $1.2 \text{ Wm}^{-2}$  absorbed by the atmosphere. The geographical distribution of all-sky surface RFP (Figure 8a) is similar to that of the TOA RFP but with enhanced negative forcing (up to  $-20 \text{ Wm}^{-2}$ ) over industrialized regions and biomass burning area characterized by large aerosol burden changes, and neighboring oceans. The clear-sky component of the surface RFP (Figure 8b) dominates over the cloudy sky component (Figure 8c). Previous studies have indicated that aerosols have a stronger impact on precipitation than well-mixed greenhouse gases because the former can effectively alter the surface shortwave flux available for evaporation [Feichter et al., 2004; Lohmann and Feichter 2005; Ming and Ramaswamy, 2009]. Consistent with the negative surface forcing, we find that

the global mean precipitation diminishes by  $0.03 \text{ mm yr}^{-1}$ , however, much of the spatial distribution of the precipitation change is insignificant (see supplementary Figure S2b).

We also assess the changes in the global mean and spatial distribution of surface air temperature, precipitation and cloud cover in response to preindustrial to present day changes in short-lived pollutant emissions. Relative to preindustrial, the present day global mean surface air temperature is simulated to decrease by only  $0.05 \text{ K}$ . Examining the spatial distribution of surface temperature change reveals that it is significant at 95% level (using student's t-test) only over  $\sim 5\%$  of the total global land area (Figure S2a), failing a field significance test. Our simulated temperature change is much less than would occur if we had not kept the SSTs constant and allowed the ocean to respond to short-lived pollutant perturbations [Hansen et al., 2005]. On a global scale, cloud cover increases by  $0.2\%$ , but the change is found to be statistically insignificant over much of the globe (Figure S2c).

## 5. Discussion and Conclusions

In this study, we have evaluated our base GFDL AM3 simulation (1980-2007 with interannually varying SSTs and SIC) against observations of key chemical species (Section 3) and have employed the model to investigate the net impact of short-lived air pollutant emission changes from preindustrial to present day on atmospheric composition and climate (Section 4). Comparison of our base simulation with observations suggests that AM3 is able to reproduce the observed tropospheric ozone seasonal cycle (pearson correlation coefficient  $r=0.45-0.97$ ) and simulated concentrations are within 10 to 15 ppbv of observed values. Surface carbon monoxide concentrations are biased low in late winter and spring compared with observations at all

northern high and mid-latitude sites similar to the multi-model biases discussed in Shindell et al. [2006a], but the observed seasonality ( $r=0.91-0.96$ ) and magnitude is captured at southern hemisphere mid and high latitudes. Tropospheric CO concentrations for 2005-2007 in our base simulation are within 15% of those observed by the TES satellite. Hydroxyl radical, the primary determinant of the tropospheric lifetime of many short-lived pollutants, is somewhat higher in our base simulation compared with climatological estimates. Consistent with high OH, our mean tropospheric methane lifetime is 8.6 years, on the lower side of published values.

Contrasting the atmospheric composition in our preindustrial (1860) and present-day (2000) simulations, both with fixed present-day sea-surface temperature, sea-ice extent, and WMGG concentrations (including methane), shows substantial increases in the present-day global total burdens of tropospheric ozone, sulfate and carbonaceous aerosols relative to preindustrial driven by short-lived pollutant emission changes. Spatially, surface ozone increases everywhere, more so in the northern hemisphere than in the southern hemisphere, mostly driven by increases in  $\text{NO}_x$  emissions. Spatially inhomogeneous changes in aerosol burdens result from the different regional trends in their emissions. For example, carbonaceous aerosol burdens decrease over North America and Europe from the preindustrial to the present day because of reduced domestic fuel burning. Uncertainties in short-lived pollutant emissions will influence our estimate of the historical changes in the abundance of ozone and aerosols. Lamarque et al. [2010] note that uncertainties in regional emissions can be larger than a factor of 2.

We simulate a 10% increase in tropospheric air-mass-weighted OH concentration for present day relative to preindustrial, indicating that increases in sources ( $\text{O}_3$ ,  $\text{NO}_x$ ) dominate over sinks ( $\text{CO}$ , NMVOCs,  $\text{SO}_2$ ) of OH. Consequently, a 14% reduction in methane lifetime is simulated for the present-day relative to preindustrial. We note that methane is set to present-day

levels in both simulations, so the potentially large impact of CH<sub>4</sub> on its own lifetime [Prather, 1996] is not included here. Analysis of our fully coupled climate-chemistry model (GFDL CM3) simulations with short-lived pollutant emissions and greenhouse gas concentrations, including CH<sub>4</sub>, evolving over the entire historical period shows that CH<sub>4</sub> lifetime increases from preindustrial to present day, demonstrating the dominant impact of CH<sub>4</sub> on its own lifetime [John et al., 2012]. Although we consider the direct influence of aerosols on gases via heterogeneous chemistry, we do not include their impact on photolysis rates, previously shown to increase the CH<sub>4</sub> lifetime by decreasing tropospheric OH [Bian et al., 2003]. In addition, we did not consider stratospheric ozone depletion from preindustrial to present-day increases in ODSs, which could modulate the changes in tropospheric ozone and aerosol burden, oxidizing capacity and therefore methane lifetime. The impacts from historical changes in ODS and CH<sub>4</sub> should be considered to estimate a more completely the full anthropogenic influence on the chemistry-climate system over the last century.

We analyze radiative forcing at the top-of-the-atmosphere, expressed as radiative flux perturbation, to estimate that substantial anthropogenic increases in tropospheric ozone and aerosols burden in the present-day relative to preindustrial cause a strong negative forcing ( $-1.43 \text{ Wm}^{-2}$ ). This finding suggests that the negative forcing (direct plus indirect) from aerosol changes dominates over the positive forcing due to O<sub>3</sub> increases and aerosol semi-direct effect, thus resulting in a net radiative cooling of the climate system. Statistically significant negative TOA forcing is concentrated over industrialized regions of the northern hemisphere characterized by high sulfate aerosol burden changes (China, India, Europe, North America). Negative forcing is enhanced at the surface and is more widespread compared with the TOA forcing. Our estimate of the TOA forcing from short-lived pollutants may be compared with estimates obtained using the

CMIP5 emissions inventory applied here. For example, Bauer et al. [2012] used this inventory to calculate a TOA forcing of  $-0.6 \text{ Wm}^{-2}$  for preindustrial to present-day changes in aerosol (or their precursor) emissions only. Our stronger negative TOA forcing compared with that of Bauer et al. [2012] could be attributed to differences in model configuration (their model included only the cloud albedo effect of aerosols). Similar experiments with other chemistry-climate models will help to determine whether this net impact of short-lived pollutants on climate since the preindustrial period is robust.

We simulate a global annual mean cooling of 0.05 K at the surface from historical changes in short-lived pollutant emissions; however this change in surface air temperature is statistically insignificant because we keep the sea-surface temperature and sea-ice extent fixed for both the preindustrial and present-day simulations – a major limitation of our study. We also do not find statistically significant changes in the total cloud cover and precipitation over most of the globe indicating that 10 year simulations are too short to produce a robust signal that can be distinguished from noise. Analysis of simulations of the GFDL CM3 with evolving sea-surface temperature and sea ice extent is currently underway to fully assess the impact of short-lived pollutants on climate [Horowitz et al. in prep, Levy et al., in prep].

## **6. Acknowledgments**

We are grateful to Simone Tilmes and Martin Schultz for kindly providing ozonesonde data and surface ozone analysis package, respectively. We thank Yuanyuan Fang, Issac Held, Jasmin John, Meiyun Lin, Yi Ming, and V. Ramaswamy for useful discussions. We appreciate helpful comments and suggestions from Songmiao Fan on an earlier version of this manuscript.

## 7. References

- Aghedo, A. M., K. W. Bowman, D. T. Shindell, and G. Faluvegi (2011), The impact of orbital sampling, monthly averaging and vertical resolution on climate chemistry model evaluation with satellite observations, *Atmos. Chem. Phys.*, *11*, 6493–6514.
- Austin, J., and J. Wilson (2010), Sensitivity of polar ozone to sea surface temperatures and halogen amounts, *J. Geophys. Res.*, *115*, D18303, doi:10.1029/2009JD013292.
- Bauer, S. E., D. Koch, N. Unger, S. M. Metzger, D. T. Shindell, and D. G. Streets (2007), Nitrate aerosols toaday and in 2030: a global simulation including aerosols and tropospheric ozone, *Atmos. Chem. Phys.*, *7*, 5043-5059, doi:10.5194/acp-7-5043-2007.
- Bauer, S. E., and S. Menon (2012), Aerosol direct, indirect, semidirect, and surface albedo effects from sector contributions based on the IPCC AR5 emissions for preindustrial and present-day conditions, *J. Geophys. Res.*, *117*, D01206, doi:10.1029/2011JD016816.
- Bellouin, N., J. Rae, A. Jones, C. Johnson, J. Haywood, and O. Boucher (2011), Aerosol forcing in the Climate Model Intercomparison Project (CMIP5) simulations by HadGEM2-ES and the role of ammonium nitrate, *J. Geophys. Res.*, *116*, D20206, doi:10.1029/2011JD016074.
- Bey I., D. J. Jacob, R. M. Yantosca, J. A. Logan, B. Field, A. M. Fiore, Q. Li, H. Liu, L. J. Mickley, and M. Schultz (2001), Global modeling of tropospheric chemistry with assimilated meteorology: Model description and evaluation, *J. Geophys. Res.*, *106*, 23,073-23,096.

782 Berntsen, T. K., I. S. A. Isaksen, G. Myhre, J. S. Fuglestedt, F. Stordal, T. A. Larsen, R. S.  
783 Freckleton, and K. P. Shine (1997), Effects of anthropogenic emissions on tropospheric  
784 ozone and its radiative forcing, *J. Geophys. Res.*, *102*, D23, 28,101-28,126.

785 Bian, H. and M. Prather (2003), Tropospheric aerosol impacts on trace gas budgets through  
786 photolysis, *J. Geophys. Res.*, *108*(D8), 4242, doi:10.1029/2002JD002743.

787 Brasseur, G. P., D. A. Hauglustaine, and S. Walters (1996), Chemical compounds in the remote  
788 Pacific troposphere: comparison between MLOPEX measurements and chemical  
789 transport model calculations, *J. Geophys. Res.*, *101*, 14,795-14,813.

790 Brasseur, G. P., et al. (1998), MOZART, a global chemical transport model for ozone and related  
791 tracers: 1. Model description, *J. Geophys. Res.*, *103*, 28265-28289.

792 Carslaw, K. S., B. P. Luo, and T. Peter (1995), An analytic expression for the composition of  
793 aqueous HNO<sub>3</sub>-H<sub>2</sub>SO<sub>4</sub> stratospheric aerosols including gas phase removal of HNO<sub>3</sub>,  
794 *Geophys. Res. Lett.*, *22*, 1877-1880.

795 Crutzen, P.J. (1973), A discussion of the chemistry of some minor constituents in the  
796 stratosphere and troposphere, *Pure Appl. Geophys.*, *106-108*, 1385-1399.

797 Crutzen, P. J. and C. Brühl (1993), A model study of atmospheric temperatures and the  
798 concentrations of ozone, hydroxyl, and some other photochemically active gases during  
799 the glacial, the preindustrial holocene, and the present, *Geophys. Res. Lett.*, *20*, 11, 1047-  
800 1050.

801 Delworth, T. L., et al. (2006), GFDL's CM2 Global Coupled Climate Models. Part I: Formulation  
802 and Simulation Characteristics, *Journal of Climate*, *19*(5), doi:10.1175/JCLI3629.1.

803 Dentener, F., S. Kinne, T. Bond, O. Boucher, J. Cofala, S. Generoso, P. Ginoux, S. Gong, J. J.  
804 Hoelzemann, A. Ito, L. Marelli, J. E. Penner, J.-P. Putaud, C. Textor, M. Schulz, G. R.  
805 van der Werf, and J. Wilson (2006), Emissions of primary aerosol and precursor gases in  
806 the years 2000 and 1750 prescribed datasets for AeroCom, *Atmos. Chem. Phys.*, **6**, 4321-  
807 4344.

808 Donner et al., The dynamical core, physical parameterizations, and basic simulation  
809 characteristics of the atmospheric component of the GFDL global coupled model CM3  
810 (2011), *J. Climate*, **24**, 3484–3519, doi: /dx.doi.org/10.1175/2011JCLI3955.

811 Duncan, B., J. A. Logan, I. Bey, I. A. Megretskaya, R. M. Yantosca, P. C. Novelli, N. B. Jones,  
812 C. P. Rinsland (2007) Global budget of CO, 1988-1997: Source estimates and validation  
813 with a global model, *J. Geophys. Res.*, **112**, D22301, doi:10.1029/2007JD008459.

814 Emmons, L. K., S. Walters, P. G. Hess, J.-F. Lamarque, G. G. Pfister, D. Fillmore, C. Granier,  
815 A. Guenther, D. Kinnison, T. Laepple, J. Orlando, X. Tie, G. Tyndall, C. Wiedinmyer, S.  
816 L. Baughcum, and S. Kloster (2010), Description and evaluation of the Model for Ozone  
817 and related chemical Tracers, version 4 (MOZART-4), *Geosci. Model Dev.*, **3**, 43-67.

818 Eyring, V., I. S. A., Isaksen, T. Berntsen, W. J. Collins, J. J. Corbett, O. Endresen, R. G.,  
819 Grainger, J. Moldanova, H. Schlager, and D. S. Stevenson (2009), Transport impacts on  
820 atmosphere and climate: Shipping, *Atmos. Environ.*,  
821 doi:10.1026/j.atmosenv.2009.04.059.

822 Fang, Y., A. M. Fiore, L. W. Horowitz, A. Gnanadesikan, I. Held, G. Chen, G. Vecchi, and H.  
823 Levy (2011), The impacts of changing transport and precipitation on pollutant

824 distributions in a future climate, *J. Geophys. Res.*, *116*, D18303,  
825 doi:10.1029/2011JD015642.

826 Feichter, J., E. Roeckner, U. Lohmann, and B. Leipert (2004), Nonlinear aspects of the climate  
827 response to greenhouse gas and aerosol forcing, *J. Clim.*, *17*, 2384-2398.

828 Fiore, A. M., D. J. Jacob, B. D. Field, D. G. Streets, S. D. Fernandes, and C. Jang (2002),  
829 Linking air pollution and climate change: The case for controlling methane, *Geophys.*  
830 *Res. Lett.*, *29*(19), 1919, doi:10.1029/2002GL015601.

831 Fiore, A. M., et al. (2009); Multimodel estimates of intercontinental source-receptor relationships  
832 for ozone pollution, *J. Geophys. Res.*, *114*, D04301, doi:10.1029/2008JD010816.

833 Folberth, G. A., D. A. Hauglustaine, J. Lathière, F. Brocheton (2006), Interactive chemistry in  
834 the Laboratoire de Météorologie Dynamique general circulation model: model  
835 description and impact analysis of biogenic hydrocarbons on tropospheric chemistry,  
836 *Atmos. Chem. Phys.*, *6*, 2273-2319.

837 Forster, P., et al. (2007), Changes in atmospheric constituents and in radiative forcing, in *Climate*  
838 *Change 2007: The Physical Science Basis. Contribution of Working Group I to the*  
839 *Fourth Assessment Report of the Intergovernmental Panel on Climate Change*, edited by  
840 S. Solomon et al., pp. 129–234, Cambridge Univ. Press, Cambridge, U. K.

841 Fuglestvedt, J. S., T. K. Berntsen, I. S. A. Isaksen, H. Mao, X.-Z. Liang, and W.-C. Wang  
842 (1999), Climatic forcing of nitrogen oxides through the changes in tropospheric ozone  
843 and methane; global 3D model studies, *Atmos. Environ.*, *33*, 961-977.

844 GFDL Global Atmospheric Model Development Team (2004), The new GFDL global  
845 atmosphere and land model AM2-LM2: evaluation with prescribed SST simulations, *J.*  
846 *Clim*, 17, 4641-4673.

847 Giorgi, F., and W. L. Chameides (1985), The rainout parameterization in a photochemical model,  
848 *J. Geophys. Res.*, 90, 7872–7880.

849 Ginoux, P., M. Chin, I. Tegen, J. M. Prospero, B. Holben, O. Dubovik, and S.-J. Lin (2001),  
850 Sources and distributions of dust aerosols simulated with the GOCART model, *J.*  
851 *Geophys. Res.*, 106, 22 255–22 274.

852 Golaz, J.-C., M. Salzmann, L. J. Donner, L. W. Horowitz, Y. Ming, and M. Zhao (2011),  
853 Sensitivity of the aerosol indirect effect to subgrid variability in the cloud  
854 parameterization of the GFDL Atmosphere General Circulation Model AM3. *J. Climate*,  
855 24(13), doi:10.1175/2010JCLI3945.1.

856 Granier, C., A. Guenther, J.-F. Lamarque, A. Mieville, J. Muller, J. Olivier, J. Orlando, J. Peters,  
857 G. Petron, G. Tyndall, and S. Wallens (2005), POET, a database of surface emissions of  
858 ozone precursors, available at: <http://www.aero.jussieu.fr/projet/ACCENT/POET.php>,  
859 2005.

860 Grenfell, J. L., D. R. Shindell, D. Koch, and D. Rind (2001), Chemistry-climate interactions in  
861 the Goddard Institute for Space Studies, general circulation model 2. New insights into  
862 modeling the preindustrial atmosphere, *J. Geophys. Res.*, 106, D24, 33,435-33,451.

863 Griffies., S. M., M. Winton, L. J. Donner, L. W. Horowitz, S. M. Downes, R. Farneti, A.  
864 Gnanadesikan, W. J. Hurlin, H. C. Lee, Z. Liang, J. B. Palter, B. L. Samuels, A. T.

865 Wittenberg, B. Wyman, J. Yin, and N. Zadeh (2011), The GFDL CM3 coupled climate  
 866 model: characteristics of the ocean and sea ice simulations, *J. Clim.*, *24*, doi:  
 867 10.1175/2011JCLI3964.1.

868 Hansen, J. E., M. Sato, R. Ruedy, A. Lacis, and V. Oinas (2000), Global warming in the twenty-  
 869 first century: An alternative scenario, *Proc. Natl. Acad. Sci.*, *97*, 9875-9880.

870 Hansen, J., et al. (2005), Efficacy of climate forcings, *J. Geophys. Res.*, *110*, D18104,  
 871 doi:10.1029/2005JD005776.

872 Hanson, D. R., and K. Mauersberger (1988), Laboratory studies of nitric acid trihydrate:  
 873 implications for the south polar stratosphere, *Geophys. Res. Lett.*, *15*, 855-858.

874 Hauglustaine, D. A., and G. P. Brasseur (2001), Evolution of tropospheric ozone under  
 875 anthropogenic activities and associated radiative forcing of climate, *J. Geophys. Res.*,  
 876 *106*, D23, 32, 337-32,360.

877 Haywood, J., L. Donner, A. Jones, J.-C. Golaz (2009), Global indirect radiative forcing caused  
 878 by aerosols: IPCC (2007) and beyond in *Clouds in the Perturbed Climate System: Their*  
 879 *relationship to energy balance, atmospheric dynamics, and precipitation* by J.  
 880 Heintzenberg and R. J. Charlson, pp. 451-567, MIT press.

881 Hess, P. G., S. Flocke, J.-F. Lamarque, M. C. Barth, and S. Madronich (2000), Episodic,  
 882 modeling of the chemical structure of the troposphere as revealed during the spring  
 883 MLOPEX 2 intensive, *J. Geophys. Res.*, *105*, doi:10.1029/2000JD900253.

884 Holloway, T., H. Levy II, and P. Kasibhatla (2000), Global distribution of carbon monoxide, *J.*  
 885 *Geophys. Res.*, *105*, D10, 12123-12147.

886 Ho, S., D. P. Edwards, J. C. Gille, M. Luo, G. B. Osterman, S. S. Kulawik, and H. Worden  
887 (2009), A global comparison of carbon monoxide profiles and column amounts from  
888 Tropospheric Emission Spectrometer (TES) and Measurements of Pollution in the  
889 Troposphere (MOPITT), *J. Geophys. Res.*, *114*, D21307, doi:10.1029/2009JD012242.

890 Horowitz, L. W., S. Walters, D. L. Mauzerall, L. K. Emmons, P. J. Rasch, C. Granier, X. Tie, J.-  
891 F. Lamarque, M. G. Schultz, G. S. Tyndall, J. J. Orlando, and G. P. Brasseur (2003), A  
892 global simulation of tropospheric ozone and related tracers: description and evaluation of  
893 MOZART, version 2, *J. Geophys. Res.*, *108*, D24, 4784, doi:10.1029/2002JD002853.

894 Horowitz, L. W. (2006), Past, present, and future concentrations of tropospheric ozone and  
895 aerosols: methodology, ozone evaluation and sensitivity to aerosol wet removal, *J.*  
896 *Geophys. Res.*, *111*, D22211, doi:10.1029/2005JD006937.

897 Horowitz, L. W., A. M. Fiore, G. P. Milly, R. C. Cohen, A. Perring, P. J. Wooldridge, P. G.  
898 Hess, L. K. Emmons, and J.-F. Lamarque (2007), Observational constraints on the  
899 chemistry of isoprene nitrates over the eastern United States, *J. Geophys. Res.*, *112*  
900 D12S08, doi:10.1029/2006JD007747.

901 Isaksen, I. S. A., et al. (2009), Atmospheric composition change: chemistry-climate interactions,  
902 *Atmos. Environ.*, *43*, 5138-5192, doi:10.1016/j.atmos.env.2009.08.003.

903 Jackson, S. C. (2009), Parallel pursuit of near-term and long-term climate mitigation, *Science*,  
904 *326*, 526-527.

905 Jaffe, D., A. Mahura, J. Kelley, J. Atkins, P. C. Novelli, and J. Merrill (1997), Impact of Asian  
 906 emissions on the remote North Pacific atmosphere: interpretation of CO data from  
 907 Shemya, Guam, Midway, and Mauna Loa, *J. Geophys. Res.*, *102*, 28,627-28,635.

908 John, J., A. M. Fiore, V. Naik, and L. W. Horowitz, and J. P. Dunne (2012), Climate versus  
 909 emission drivers of methane lifetime from 1860-2100, *submitted to Atmos. Chem. Phys.*

910 Jöckel, P., H. Tost, A. Pozzer, C. Brühl, J. Buchholz, L. Ganzeveld, P. Hoor, A. Kerkweg, M. G.  
 911 Lawrence, R. Sander, B. Steil, G. Stiller, M. Tanarhte, D. Taraborrelli, J. van Aardenne,  
 912 and J. Lelieveld (2006), The atmospheric chemistry general circulation model  
 913 ECAM5/MESSy1: consistent simulation of ozone from the surface to the mesosphere,  
 914 *Atmos. Chem. Phys.*, *6*, 5067-5104.

915 Kanakidou, et al. (2005), Organic aerosol and global climate modeling: a review, *Atmos. Chem.*  
 916 *Phys.*, *5*, 1053-1123, 1680-7324/acp/2005-5-1053.

917 Krol, M., P. J. van Leeuwen, and J. Lelieveld (1998), Global OH trend inferred from methyl  
 918 chloroform measurements, *J. Geophys. Res.*, *103*, D9, 10697-10711.

919 Krol, M., and J. Lelieveld (2003), Can the variability in tropospheric OH be deduced from  
 920 measurements of 1,1,1-trichloroethane (methyl chloroform)? *J. Geophys. Res.*, *108*(D3),  
 921 doi:10.1029/2002JD002423.

922 Kulawik, S. S., J. Worden, A. Eldering, K. Bowman, M. Gunson, G. B. Osterman, L. Zhang, S.  
 923 Clough, M. W. Shephard, and R. Beer (2006), Implementation of cloud retrievals for  
 924 Tropospheric Emission Spectrometer (TES) atmospheric retrievals: part 1. Description

925 and characterization of errors on trace gas retrievals, *J. Geophys. Res.*, *111*, D24204,  
 926 doi:10.1029/2005JD006733.

927 Lamarque, J.-F., J. T. Kiehl, P. G. Hess, W. D. Collins, L. K. Emmons, P. Ginoux, C. Luo, and  
 928 X. X. Tie (2005a), Response of a coupled chemistry-climate model to changes in aerosol  
 929 emissions: Global impact on the hydrological cycle and the tropospheric burden of OH,  
 930 ozone, and NO<sub>x</sub>, *Geophys. Res. Lett.*, *32*, L16809, doi:10.1029/2005GL023419.

931 Lamarque, J.-F., P. Hess, L. Emmons, L. Buja, W. Washington, and C. Granier (2005b),  
 932 Tropospheric ozone evolution between 1890 and 1990, *J. Geophys. Res.*, *110*, D08304,  
 933 doi:10.1029/2004JD005537.

934 Lamarque, J.-F., T. C. Bond, V. Eyring, C. Granier, A. Heil, Z. Klimont, D. Lee, C. Liousse, A.  
 935 Mieville, B. Owen, M. G. Schultz, D. Shindell, S. J. Smith, E. Stehfest, J. Van Aardenne,  
 936 O. R. Cooper, M. Kainuma, N. Mahowald, J. R. McConnell, V. Naik, K. Riahi, and D. P.  
 937 van Vuuren (2010), Historical (1850–2000) gridded anthropogenic and biomass burning  
 938 emissions of reactive gases and aerosols: methodology and application, *Atmos. Chem.*  
 939 *Phys. Discuss.*, *10*, 4963-5019.

940 Lawrence, M. G., P. Jöckel, and R. von Kuhlmann (2001), What does the global mean OH  
 941 concentration tell us?, *Atmos. Phys. Chem.*, *1*, 37-49.

942 Lee, D. S., B. Owen, A. Graham, C. Fichter, L. L. Lin, and D. Dimitriu (2005), Allocation of  
 943 International Aviation emissions from scheduled air traffic – present day and historical  
 944 (Report 2 of 3), Manchester Metropolitan University, Center for Air Transport and the  
 945 Environment, CATE-2005-3(C)-2, Manchester, UK.

946 ([http://www.cate.mmu.ac.uk/documents/projects/mmuallocationsreport2currentdayv1\\_5.](http://www.cate.mmu.ac.uk/documents/projects/mmuallocationsreport2currentdayv1_5.pdf)  
 947 [pdf](#)).

948 Lelieveld, J., W. Peters, F. J. Dentener, and M. C. Krol (2002), Stability of tropospheric hydroxyl  
 949 chemistry, *J. Geophys. Res.*, *107*, D23, doi:10.1029/2002JD002272.

950 Lelieveld, J., F. J. Dentener, W. Peters, and M. C. Krol (2004), On the role of hydroxyl radicals  
 951 in the self-cleansing capacity of the troposphere, *Atmos. Chem. Phys.*, *4*, 2337-2344.

952 Levy II, H. (1971), Normal atmosphere: Large radical and formaldehyde concentrations  
 953 predicted, *Science*, *173*, 141-143.

954 Levy II, H., M Daniel Schwarzkopf, L. W Horowitz, V. Ramaswamy, and K. L. Findell (2008),  
 955 Strong sensitivity of late 21st Century climate to projected changes in short-lived air  
 956 pollutants, *J. Geophys. Res.*, *113*, D06102, DOI:10.1029/2007JD009176.

957 Li, F., P. Ginoux, and V. Ramaswamy (2008), Distribution, transport, and deposition of mineral  
 958 dust in the Southern Ocean and Antarctica: contribution of major sources, *J. Geophys.*  
 959 *Res.*, *113*, D10207, doi:10.1029/2007JD009190.

960 Liao, H., Y. Zhang, W.-T. Chen, F. Raes, and J. H. Seinfeld (2009), Effect of chemistry-aerosol-  
 961 coupling on predictions of future climate and future levels of tropospheric ozone and  
 962 aerosols, *J. Geophys. Res.*, *114*, D10306, doi:10.1029/2008JD010984.

963 Li, M., A. M. Fiore, L. W. Horowitz, O. Cooper, V. Naik, J. S. Holloway, B. J. Johnson, A.  
 964 Middlebrook, S. J. Oltmans, I. B. Pollack, T. B. Ryerson, J. X. Warner, C. Wiedinmyer,  
 965 R. J. Wilson, and B. Wyman (2012), Transport of Asian ozone pollution into surface air

966 over the western United States in spring, *J. Geophys. Res.*, *117*, D00V07, doi:  
 967 10.1029/2011JD016961.

968 Liu, H., D.J. Jacob, I. Bey, and R.M. Yantosca (2001), Constraints from  $^{210}\text{Pb}$  and  $^7\text{Be}$  on wet  
 969 deposition and transport in a global three-dimensional chemical tracer model driven by  
 970 assimilated meteorological fields, *J. Geophys. Res.*, *106(D11)*, 12,109-12,128.

971 Logan, J. A., M. J. Prather, S. C. Wofsy, and M. B. McElroy (1981), Tropospheric chemistry: a  
 972 global perspective, *J. Geophys. Res.*, *86*, C8, 7210-7254.

973 Logan, J. A. (1999), An analysis of ozonesonde data for the troposphere: Recommendations for  
 974 testing 3-D models, and development of a gridded climatology for tropospheric ozone, *J.*  
 975 *Geophys. Res.*, *104*, 16,115-16,149.

976 Lohmann, U., and J. Feichter (2005), Global indirect aerosol effects: a review, *Atmos. Chem.*  
 977 *Phys.*, *5*, 715-737.

978 Lohmann, U., L. Rotstajn, T. Storelvmo, A. Jones, S. Menon, J. Quaas, A. M. L. Ekman, D.  
 979 Koch, and R. Ruedy (2010), Total aerosol effect: radiative forcing or radiative flux  
 980 perturbation?, *Atmos. Chem. Phys.*, *10*, 3235-3246.

981 Lopez, J. P., M. Luo, L. E. Christensen, M. Loewenstein, H. Jost, C. R. Webster, and G.  
 982 Osterman (2008), TES carbon monoxide validation during two AVE campaigns using the  
 983 Argus and ALIAS instruments on NASA's WB-57F, *J. Geophys. Res.*, *113*, D16S47,  
 984 doi:10.1029/2007JD008811.

985 Luo, M., et al. (2007a), Comparison of carbon monoxide measurements by TES and MOPITT:  
 986 Influence of in situ data and instrument characteristics on nadir atmospheric species  
 987 retrievals, *J. Geophys. Res.*, *112*, D09303, doi:10.1029/2006JD007663.

988 Luo, M., et al. (2007b), TES carbon monoxide validation with DACOM aircraft measurements  
 989 during INTEx-B 2006, *J. Geophys. Res.*, *112*, D24S48, doi:10.1029/2007JD008803.

990 Madronich, S., and S. Flocke (1998), *The role of solar radiation in atmospheric chemistry*,  
 991 Handbook of Environmental Chemistry, P. Boule, ed., Springer-Verland, Heidelberg, pp  
 992 1-26.

993 Mahowald, N., D. S. Ward, S. Kloster, M. G. Flanner, C. L. Heald, N. G. Heavens, P. G. Hess,  
 994 J.-F. Lamarque, and P. Y. Chuang (2011), Aerosol impacts on climate and  
 995 biogeochemistry, *Ann. Rev. Environ. Res.*, *36*, 10.1146/annurev-environ-042009-094507.

996 Martin, R.V., D. J. Jacob, R. M. Yantosca, M. Chin, and P. Ginoux (2003), Global and regional  
 997 decreases in tropospheric oxidants from photochemical effects of aerosols, *J. Geophys.*  
 998 *Res.*, *108(D3)*, 4097, doi:10.1029/2002JD002622.

999 Martinerie, P., G. P. Brasseur, and C. Granier (1995), The chemical composition of ancient  
 1000 atmospheres: a model study constrained by ice core data, *J. Geophys. Res.*, *100*, D7,  
 1001 14,291-14,304.

1002 Meinshausen, M., S. J. Smith, K. V. Calvin, J. S. Daniel, M. Kainuma, J.-F. Lamarque, K.  
 1003 Matsumoto, S. A. Montzka, S. C. B. Raper, K. Riahi, A. M. Thomson, G. J. M. Velders  
 1004 and D. van Vuuren (2011), The RCP Greenhouse Gas Concentrations and their Extension  
 1005 from 1765 to 2300, Climatic Change (Special Issue), doi:10.1007/s10584-011-0156-z.

1006 Menon, S., N. Unger, D. Koch, J. Francis, T. Garrett, I. Sednev, D. Shindell, and D. Streets  
 1007 (2008), Aerosol climate effects and air quality impacts from 1980 to 2030. *Environ. Res.*  
 1008 *Lett.*, 3, 024004, doi:10.1088/1748-9326/3/2/024004.

1009 Mickley, L. J., P. P. Murti, D. J. Jacob, J. A. Logan, D. M. Koch, and D. Rind (1999), Radiative  
 1010 forcing from tropospheric ozone calculated with a unified chemistry-climate model, *J.*  
 1011 *Geophys. Res.*, 104, D23, 30,153-30,172.

1012 Ming, Yi, and V Ramaswamy (2009), Nonlinear climate and hydrological responses to aerosol  
 1013 effects, *J. Climate*, 22(6), 1329-1339.

1014 Molina, M., D. Zaelke, K. Madhava Sarma, S. O. Andersen, V. Ramanathan, and D. Kaniaru  
 1015 (2009), Reducing abrupt climate change risk using the Montreal Protocol and other  
 1016 regulatory actions to complement cuts in CO2 emissions, *Proc. Natl. Acad. Sci.*, 106,  
 1017 20616-20621.

1018 Monahan, E. C., D. E. Spiel, and K. L. Davidsona (1986), A model of marine aerosol generation  
 1019 via whitecaps and wave disruption, *Oceanic Whitecaps*, E. C. Monahan and G. Mac  
 1020 Niocaill, Eds., D. Reidel, 167–174.

1021 Montzka, S. A., C. M. Spivakovsky, J. H. Butler, J. W. Elkins, L. T. Lock, and D. J. Mondeel  
 1022 (2000), New observational constraints, for atmospheric hydroxyl on global and  
 1023 hemispheric scales, *Science*, 288, 500-503.

1024 Montzka, S. A., M. Krol, E. Dlugokencky, B. Hall, P. Jöckel, and J. Lelieveld (2011), Small  
 1025 interannual variability of global atmospheric hydroxyl, *Science*, 331, 67-69.

1026 Naik, V., D. Mauzerall, L. Horowitz, D. Schwarzkopf, V. Ramaswamy, and M. Oppenheimer  
 1027 (2005), Net radiative forcing due to changes in regional emissions of tropospheric ozone  
 1028 precursors, *J. Geophys. Res.*, *110*, doi:10.1029/2005JD005908.

1029 Nassar, R., et al. (2008), Validation of Tropospheric Emission Spectrometer (TES) Nadir Ozone  
 1030 Profiles Using Ozonesonde Measurements, *J. Geophys. Res.*, *113*, D15S17,  
 1031 doi:10.1029/2007JD008819.

1032 Novelli, P. C., K. A. Masarie, and P. M. Lang (1998), Distributions and recent changes of carbon  
 1033 monoxide in the lower troposphere, *J. Geophys. Res.*, *103*, 19,015-19,033.

1034 Novelli, P.C. and K.A. Masarie (2010), Atmospheric Carbon Monoxide Dry Air Mole Fractions  
 1035 from the NOAA ESRL Carbon Cycle Cooperative Global Air Sampling Network, 1988-  
 1036 2009, Version: 2010-07-14, path: <ftp://ftp.cmdl.noaa.gov/ccg/co/flask/event/>  
 1037 (downloaded on August 10, 2010).

1038 Penner, J. E., M. J. Prather, I. S. A. Isaksen, J. S. Fuglestad, Z. Klimont and D. S. Stevenson  
 1039 (2010), Short-lived uncertainty? *Nature Geosci.*, *3*, 587-588.

1040 Prather, M.J. (1996), Natural modes and time scales in atmospheric chemistry: Theory, GWPs  
 1041 for CH<sub>4</sub> and CO, and runaway growth, *Geophys. Res. Lett.*, *23*, 2597-2600.

1042 Prather, M. J., D. Ehhalt, F. Dentener, et al. (2001), Atmospheric chemistry and greenhouse  
 1043 gases, in *Climate Change 2001: The Scientific Basis. Contribution of Working Group I to*  
 1044 *the Third Assessment Report of the Intergovernmental Panel on Climate Change*, edited  
 1045 by J. T. Houghton, et al., pp 239-287, Cambridge Univ. Press, New York.

1046 Prinn, R. G., R. F. Weiss, B. R. Miller, J. Huang, F. N. Alyea, D. M. Cunnold, P. J. Fraser, D. E.  
 1047 Hartley, and P. G. Simmonds (1995), Atmospheric trends and lifetime of CH<sub>3</sub>CCl<sub>3</sub> and  
 1048 global OH concentrations, *Science*, 269, 187.

1049 Prinn, R., J. Huang, R. F. Weiss, D. M. Cunnold, P. J. Fraser, P. G. Simmonds, A. McCullough,  
 1050 C. Harth, P. Salameh, S. O'Doherty, R. H. J. Wang, L. Porter, and B. R. Miller (2001),  
 1051 Evidence for substantial variations of atmospheric hydroxyl radicals in the past two  
 1052 decades, *Science*, 292, 1882.

1053 Rasmussen, D. J., A. M. Fiore, V. Naik, L. W. Horowitz, S. J. McGinnis, and M. G. Schultz  
 1054 (2012), Surface ozone-temperature relationships in the eastern US: a monthly  
 1055 climatology for evaluating chemistry-climate models, *Atmos. Environ.*, 47, doi:  
 1056 10.1016/j.atmosenv.2011.11.021.

1057 Rayner, N. A., D. E. Parker, E. B. Horton, C. K. Folland, L. V. Alexander, and D. P. Rowell  
 1058 (2003), Global analyses of sea surface temperature, sea ice, and night marine air  
 1059 temperature since the late nineteenth century, *J. Geophys. Res.*, 108,  
 1060 doi:10.1029/2002JD002670.

1061 Richards, N. A. D., Q. Li, K. W. Bowman, J. R. Worden, S. S. Kulawik, G. B. Osterman, H. M.  
 1062 Worden, J.-F., Lamarque, and B. V. Khattatov (2006), Assimilation of TES CO into a  
 1063 global CTM: first results, *Atmos. Chem. Phys. Discuss.*, 6, 11,727-11,723.

1064 Rosenfeld, D., U. Lohmann, G. B. Raga, C. O'Dowd, M. Kulmala, S. Fuzzi, A. Reissell, M. O.  
 1065 Andreae (2008), Flood or drought: how do aerosols affect precipitation?, *Science*, 321,  
 1066 1309-1313.

1067 Sander, S. P., R. R. Friedl, D. M. Golden, M. J. Kurylo, G. K. Moortgat, H. Keller-Rudek, P. H.  
 1068 Wine, A. R. Ravishankara, C. E. Kolb, M. J. Molina, B. J. Finlayson-Pitts, R. E. Huie,  
 1069 and V. L. Orkin, *Chemical kinetics and photochemical data for use in atmospheric*  
 1070 *studies*, Evaluation No. 15, JPL Publications 06-2, 2006, Jet Propulsion Laboratory,  
 1071 Pasadena, CA, USA.

1072 Shindell, D. T., G. Faluvegi, and N. Bell (2003), Preindustrial-to-present-day radiative forcing by  
 1073 tropospheric ozone from improved simulations with the GISS chemistry-climate GCM.  
 1074 *Atmos. Chem. Phys.*, *3*, 1675-1702, doi:10.5194/acp-3-1675-2003.

1075 Shindell, D. T., et al. (2006a), Multimodel simulations of carbon monoxide: Comparison with  
 1076 observations and projected near-future changes, *J. Geophys. Res.*, *111*, D19306,  
 1077 doi:10.029/2006JD007100.

1078 Shindell, D. T., G. Faluvegi, N. Unger, E. Aguilar, G. A. Schmidt, D. M. Koch, S. E. Bauer, and  
 1079 R. L. Miller (2006b), Simulations of preindustrial, present-day, and 2100 conditions in  
 1080 the NASA GISS composition and climate model G-PUCCINI, *Atmos. Chem. Phys.*, *6*,  
 1081 4427-4459.

1082 Shindell, D. T., G. Faluvegi, S. E. Bauer, D. Koch, N. Unger, S. Menon, R. L. Miller, G. A.  
 1083 Schmidt, and D. G. Streets (2007), Climate response to projected changes in short-lived  
 1084 species under the A1B scenario from 2000-2050 in the GISS climate model. *J. Geophys.*  
 1085 *Res.*, *112*, D20103, doi:10.1029/2007JD008753.

1086 Shindell, D. T., H. Levy, II, M. D. Schwarzkopf, L. W. Horowitz, J.-F. Lamarque, and G.  
 1087 Faluvegi (2008), Multimodel projections of climate change from short-lived emissions  
 1088 due to human activities. *J. Geophys. Res.*, *113*, D11109, doi:10.1029/2007JD009152.

1089 Shindell, D. T. and J.-F. Lamarque (2011), The atmospheric Chemistry and Climate Model Inter-  
 1090 comparison Project (ACCMIP), *IGAC News*, 45, 9-14.

1091 Shindell, D., J. C. I. Kuylenstierna, E. Vignati, R. van Dingenen, M. Amann, Z. Klimont, S. C.  
 1092 Anenberg, N. Muller, G. Janssens-Maenhout, F. Raes, J. Schwartz, G. Faluvegi, L.  
 1093 Pozzoli, K. Kupiainen, L. Höglund-Isaksson, L. Emberson, D. Streets, V. Ramanathan,  
 1094 K. Hicks, N. T. K. Oanh, G. Milly, M. Williams, V. Demkine, and D. Fowler (2012),  
 1095 Simultaneously mitigating near-term climate change and improving human health and  
 1096 food security, *Science*, 335, 183-189, doi:10.1126/science.1210026.

1097 Skeie, R. B., T. K. Berntsen, G. Myhre, K. Tanaka, M. M. Kvalevåg, and C. R. Hoyle (2011),  
 1098 Anthropogenic radiative forcing time series from pre-industrial times until 2010, *Atmos.*  
 1099 *Chem. Phys.*, 11, doi:10.5194/acp-11-11827-2011.

1100 Sofen, E. D., B. Alexander, and S. A. Kunasek (2011), The impact of anthropogenic emissions  
 1101 on atmospheric sulfate production pathways, oxidants, and ice core  $\Delta^{17}\text{O}(\text{SO}_4^{-2})$ , *Atmos.*  
 1102 *Chem. Phys.*, 11, doi:10.5194/acp-11-3565-2011.

1103 Stevenson, D. S., F. J. Dentener, M. Schultz, et al. (2006), Multi-model ensemble simulations of  
 1104 present-day and near-future tropospheric ozone, *J. Geophys. Res.*, 111, D08301,  
 1105 doi:10.1029/2005JD006338.

1106 Spivakovsky, C. M., J. A. Logan, S. A., Montzka, Y. J. Balkanski, M. Foreman-Fowler, D. B. A.  
 1107 Jones, L. W. Horowitz, A. C. Fusco, C. A. M. Brenninkmeijer, M. J. Prather, S. C.  
 1108 Wofsy, and M. B. McElroy (2000), Three-dimensional climatological distribution of  
 1109 tropospheric OH: Update and evaluation, *J. Geophys. Res.*, 105, D7, 8931-8980.

1110 Thompson, A. M. (1992), The oxidizing capacity of the Earth's atmosphere: Probable past and  
 1111 future changes, *Science*, 256, 1157-1165.

1112 Tie, X.X., S. Madronich, S. Walters, D. P. Edwards, P. Ginoux, N. Mahowald, R. Y. Zhang, C.  
 1113 Lou, and G. Brasseur (2005), Assessment of the global impact of aerosols on  
 1114 tropospheric oxidants, *J. Geophys. Res.*, 110, D03204, doi:10.1029/2004JD005359.

1115 Tilmes, S., J.-F. Lamarque, L. K. Emmons, A. Conley, M. G. Schultz, M. Saunois, V. Thouret,  
 1116 A. M. Thompson, S. J. Oltmas, B. Johnson, and D. Tarasick (2011), Ozone-sonde  
 1117 climatology between 1995 and 2009: description, evaluation, and applications, *Atmos.*  
 1118 *Chem. Phys. Discuss.*, 11, doi:10.5194/acpd-11-28747-2011.

1119 Tsigaridis, K., M. Krol, F.J. Dentener, Y. Balkanski, J. Lathière, S. Metzger, D.A. Hauglustaine,  
 1120 and M. Kanakidou (2006), Change in global aerosol composition since preindustrial  
 1121 times, *Atmos. Chem. Phys.*, 6, 5143-5162, doi:10.5194/acp-6-5143-2006.

1122 Unger, N., D. T. Shindell, D. M. Koch, and D. G. Streets (2006), Cross influences of ozone and  
 1123 sulfate precursor emissions changes on air quality and climate, *Proc. Natl. Acad. Sci.*,  
 1124 103, 4377-4380, doi:10.1073/pnas.0508769103.

1125 Unger, N., S. Menon, D.M. Koch, and D.T. Shindell (2009), Impacts of aerosol-cloud  
 1126 interactions on past and future changes in tropospheric composition, *Atmos. Chem. Phys.*,  
 1127 9, 4155-4129, doi:10.5194/acp-9-4115-2009.

1128 Van der Werf, G. R., J. T. Randerson, L. Giglio, G. J. Collatz, P. S. Kasibhatla, A. F. Arellano  
 1129 (2006), Interannual variability in global biomass burning emissions from 1997 to 2004,  
 1130 *Atmos. Chem. Phys.*, 6, 3423-3441.

1131 Wang, Y., and D. J. Jacob (1998), Anthropogenic forcing on tropospheric ozone and OH since  
 1132 preindustrial times, *J. Geophys. Res.*, *103*, 31,123-31,135.

1133 Wang, Y., J. A. Logan, and D. J. Jacob (1998), Global simulation of tropospheric O<sub>3</sub>-NO<sub>x</sub>-  
 1134 hydrocarbon chemistry, 2. Model evaluation and global ozone budget, *J. Geophys. Res.*,  
 1135 *103(D9)*, 10,727-10,756.

1136 Wesely, M. L. (1989), Parameterization of surface resistance to gaseous dry deposition in  
 1137 regional-scale numerical models, *Atmos. Environ.*, *23*, 1293-1304.

1138 West, J. J., A. M. Fiore, V. Naik, L. W. Horowitz, M. D. Schwarzkopf, and D. L. Mauzerall  
 1139 (2007), Ozone air quality and radiative forcing consequences of changes in ozone  
 1140 precursor emissions, *Geophys. Res. Lett.*, *34*, L06806, 10.1029/2006GL029173.

1141 Wild, O. (2007), Modeling the global tropospheric ozone budget: exploring the variability in  
 1142 current models, *Atmos. Chem. Phys.*, *7*, doi:10.5194/acp-7-2643-2007, 2643-2660.

1143 Wild, O., M. J. Prather, and H. Akimoto (2001), Indirect long-term global radiative cooling from  
 1144 NO<sub>x</sub> emissions, *Geophys. Res. Lett.*, *28*, 1719-1722.

1145 Wong, S., W.-C. Wang, I. S. A. Isaksen, T. K. Berntsen, and J. K. Sundet (2004), A global  
 1146 climate-chemistry model study of present-day tropospheric chemistry and radiative  
 1147 forcing from changes in tropospheric O<sub>3</sub> since the preindustrial period, *J. Geophys. Res.*,  
 1148 *109*, D11309, doi:10.1029/2003JD003998.

1149

1150 **Tables**

1151 Table 1. Chemical species included in AM3. Soluble gaseous species that undergo wet  
 1152 deposition in AM3 are marked with an asterisk (\*).

| No.                | Species Name | Chemical Formula   | Details                         |
|--------------------|--------------|--|---------------------------------|
| <b>Transported</b> |              |  |                                 |
| 1                  | O3           | O <sub>3</sub>   | ozone                           |
| 2                  | N2O          | N <sub>2</sub> O   | nitrous oxide                   |
| 3                  | NO           | NO   | nitric oxide                    |
| 4                  | NO2          | NO <sub>2</sub>  | nitrogen dioxide                |
| 5                  | NO3          | NO <sub>3</sub>  | nitrate radical                 |
| 6                  | HNO3*        | HNO <sub>3</sub>   | nitric acid                     |
| 7                  | HO2NO2*      | HNO <sub>4</sub>   | pernitric acid                  |
| 8                  | N2O5         | N <sub>2</sub> O <sub>5</sub>                                    | dinitrogen pentaoxide           |
| 9                  | CH4          | CH <sub>4</sub>  | methane                         |
| 10                 | CH3OOH       | CH <sub>3</sub> OOH  | methyl hydroperoxide            |
| 11                 | CH2O*        | HCHO   | formaldehyde                    |
| 12                 | CO           | CO   | carbon monoxide                 |
| 13                 | H2O2*        | H <sub>2</sub> O <sub>2</sub>                                    | hydrogen peroxide               |
| 14                 | C3H6         | C <sub>3</sub> H <sub>6</sub>                                    | propene                         |
| 15                 | ISOP         | C <sub>5</sub> H <sub>8</sub>                                    | isoprene                        |
| 16                 | CH3CHO*      | CH <sub>3</sub> CHO  | acetaldehyde                    |
| 17                 | POOH*        | C <sub>3</sub> H <sub>6</sub> OHOOH                              |                                 |
| 18                 | CH3COOOH*    | CH <sub>3</sub> COOOH  | peracetic acid                  |
| 19                 | PAN          | CH <sub>3</sub> CO <sub>3</sub> NO <sub>2</sub>                  | peroxy acetyl nitrate           |
| 20                 | ONIT*        | CH <sub>3</sub> COCHO <sub>2</sub> CH <sub>2</sub> OHNO          |                                 |
| 21                 | C2H6         | C <sub>2</sub> H <sub>6</sub>                                    | ethane                          |
| 22                 | C2H4         | C <sub>2</sub> H <sub>4</sub>                                    | ethene                          |
| 23                 | C4H10        | C <sub>4</sub> H <sub>10</sub>                                   | lumped alkanes as C ≥ 4         |
| 24                 | MPAN         | CH <sub>2</sub> CCH <sub>3</sub> CO <sub>3</sub> NO <sub>2</sub> | methacryloyl peroxy nitrate     |
| 25                 | MVK*         | CH <sub>2</sub> CHCOCH <sub>3</sub>                              | methyl vinyl ketone             |
| 26                 | MACR*        | CH <sub>2</sub> CCH <sub>3</sub> CHO                             | methacrolein                    |
| 27                 | MACROOH*     | CH <sub>3</sub> COCH(OOH)CH <sub>2</sub> OH                      |                                 |
| 28                 | C2H5OOH*     | C <sub>2</sub> H <sub>5</sub> OOH                                | ethyl hydroperoxide             |
| 29                 | C10H16       | C <sub>10</sub> H <sub>16</sub>                                  | lumped monoterpenes as α-pinene |
| 30                 | C3H8         | C <sub>3</sub> H <sub>8</sub>                                    | propane                         |
| 31                 | C3H7OOH*     | C <sub>3</sub> H <sub>7</sub> OOH                                | propyl hydroperoxide            |
| 32                 | CH3COCH3     | CH <sub>3</sub> COCH <sub>3</sub>                                | acetone                         |
| 33                 | ROOH*        | CH <sub>3</sub> COCH <sub>2</sub> OOH                            |                                 |
| 34                 | CH3OH*       | CH <sub>3</sub> OH   | methanol                        |
| 35                 | C2H5OH*      | C <sub>2</sub> H <sub>5</sub> OH                                 | ethanol                         |
| 36                 | GLYALD*      | HOCH <sub>2</sub> CHO  | glycolaldehyde                  |
| 37                 | HYAC*        | CH <sub>3</sub> COCH <sub>2</sub> OH                             | hydroxyacetone                  |

|    |                                 |  |  |
|----|---------------------------------|--|--|
| 38 | HYDRALD*                        | HOCH <sub>2</sub> CCH <sub>3</sub> CHCHO                               | lumped unsaturated hydroxycarbonyl     |
| 39 | CH <sub>3</sub> COCHO*          | CH <sub>3</sub> COCHO  | methyl glyoxal                         |
| 40 | ONITR*                          | CH <sub>2</sub> CCH <sub>3</sub> CHONO <sub>2</sub> CH <sub>2</sub> OH | lumped isoprene nitrate                |
| 41 | XOOH*                           | HOCH <sub>2</sub> C(OOH)CH <sub>3</sub> CH(OH)CHO                      |  |
| 42 | ISOPOOH*                        | HOCH <sub>2</sub> C(OOH)CH <sub>3</sub> CHCH <sub>2</sub>              | unsaturated hydroxyhydroperoxide       |
| 43 | H <sub>2</sub>                  | H <sub>2</sub>   | molecular hydrogen                     |
| 44 | SO <sub>2</sub> *               | SO <sub>2</sub>  | sulfur dioxide                         |
| 45 | SO <sub>4</sub>                 | SO <sub>4</sub> <sup>2-</sup>  | sulfate                                |
| 46 | DMS*                            | CH <sub>3</sub> SCH <sub>3</sub>                                       | dimethyl sulfide                       |
| 47 | NH <sub>3</sub> *               | NH <sub>3</sub>  | ammonia                                |
| 48 | NH <sub>4</sub> NO <sub>3</sub> | NH <sub>4</sub> NO <sub>3</sub>  | ammonium nitrate                       |
| 49 | NH <sub>4</sub>                 | NH <sub>4</sub> <sup>+</sup>   | ammonium                               |
| 50 | SOA                             |  | secondary organic aerosol              |
| 51 | dust1                           | dust   | dust dry radius 0.1 – 1.0 μm           |
| 52 | dust2                           | dust   | dust dry radius 1.0 – 1.8 μm           |
| 53 | dust3                           | dust   | dust dry radius 1.8 – 3.0 μm           |
| 54 | dust4                           | dust   | dust dry radius 3.0 – 6.0 μm           |
| 55 | dust5                           | dust   | dust dry radius 6.0 – 10.0 μm          |
| 56 | ssalt1                          | sea salt   | sea salt dry radius 0.1 – 1.0 μm       |
| 57 | ssalt2                          | sea salt   | sea salt dry radius 1.0 – 1.8 μm       |
| 58 | ssalt3                          | sea salt   | sea salt dry radius 1.8 – 3.0 μm       |
| 59 | ssalt4                          | sea salt   | sea salt dry radius 3.0 – 6.0 μm       |
| 60 | ssalt5                          | sea salt   | sea salt dry radius 6.0 – 10.0 μm      |
| 61 | bcphob                          | black carbon   | hydrophobic fraction of black carbon   |
| 62 | bcphil                          | black carbon   | hydrophilic fraction of black carbon   |
| 63 | omphob                          | organic matter   | hydrophobic fraction of organic matter |
| 64 | omphil                          | organic matter   | hydrophilic fraction of organic matter |
| 65 | HCl*                            | HCl  | hydrochloric acid                      |
| 66 | HOCl                            | HOCl   | hypochlorous acid                      |
| 67 | ClONO <sub>2</sub>              | ClONO <sub>2</sub>   | chlorine nitrate                       |
| 68 | Cl                              | Cl   | elemental chlorine                     |
| 69 | ClO                             | ClO  | chlorine monoxide                      |
| 70 | Cl <sub>2</sub> O <sub>2</sub>  | Cl <sub>2</sub> O <sub>2</sub>   | chlorine monoxide dimer                |
| 71 | Cl <sub>2</sub>                 | Cl <sub>2</sub>  | molecular chlorine                     |
| 72 | HOBr                            | HOBr   | hypobromous acid                       |
| 73 | HBr*                            | HBr  | hydrobromic acid                       |
| 74 | BrONO <sub>2</sub>              | BrONO <sub>2</sub>   | bromine nitrate                        |
| 75 | Br                              | Br   | elemental bromine                      |
| 76 | BrO                             | BrO  | bromine monoxide                       |
| 77 | BrCl                            | BrCl   | bromine monochloride                   |
| 78 | H <sub>2</sub> O                | H <sub>2</sub> O   | water                                  |

| Not transported |         |   |  |
|-----------------|---------|---|--|
| 79              | O       | O( <sup>3</sup> P)  | ground state atomic oxygen                   |
| 80              | O1D     | O( <sup>1</sup> D)  | excited state atomic oxygen                  |
| 81              | OH      | OH  | hydroxyl radical                             |
| 82              | HO2     | HO <sub>2</sub>   | hydroperoxyl radical                         |
| 83              | CH3O2   | CH <sub>3</sub> O <sub>2</sub>  | methyl peroxy radical                        |
| 84              | ISOPO2  | HOCH <sub>2</sub> C(OO)CH <sub>3</sub> CHCH <sub>2</sub>              | peroxy radical derived from OH+ISOP          |
| 85              | CH3CO3  | CH <sub>3</sub> CO <sub>3</sub>                                       | acetylperoxy radical                         |
| 86              | MACRO2  | CH <sub>3</sub> COCH(OO)CH <sub>2</sub> OH                            | peroxy radical from OH addition to MVK, MACR |
| 87              | EO2     | HOCH <sub>2</sub> CH <sub>2</sub> O <sub>2</sub>                      |  |
| 88              | EO      | HOCH <sub>2</sub> CH <sub>2</sub> O                                   |  |
| 89              | MCO3    | CH <sub>2</sub> CCH <sub>3</sub> CO <sub>3</sub>                      | peroxy radical from reaction of OH with MACR |
| 90              | RO2     | CH <sub>3</sub> COCH <sub>2</sub> O <sub>2</sub>                      | 1-methyl vinoxy radical                      |
| 91              | C2H5O2  | C <sub>2</sub> H <sub>5</sub> O <sub>2</sub>                          | ethyl peroxy radical                         |
| 92              | ISOPNO3 | CH <sub>2</sub> CHCCH <sub>3</sub> OOCH <sub>2</sub> ONO <sub>2</sub> | peroxy isoprene nitrate                      |
| 93              | XO2     | HOCH <sub>2</sub> C(OO)CH <sub>3</sub> CH(OH)CHO                      | Peroxy radical from OH+HYDRALD               |
| 94              | PO2     | C <sub>3</sub> H <sub>6</sub> OHO <sub>2</sub>                        |  |
| 95              | C3H7O2  | C <sub>3</sub> H <sub>7</sub> O <sub>2</sub>                          | propyl peroxy radical                        |
| 96              | H       | H   | hydrogen                                     |
| 97              | N       | N   | elemental nitrogen                           |

1153

Table 2. Emissions of short-lived species in AM3 for year 2000. Emissions for year 1860 are shown in parentheses.

| Species   | Anthropogenic                         | Biomass Burning | Biogenic/Soil | Oceans      | Ship       | Total          |
|---|---------------------------------------|-----------------|---------------|-------------|------------|----------------|
| NO <sub>x</sub> (Tg N yr <sup>-1</sup> )                | 26.5 (0.7)                            | 5.5 (4.8)       | 3.6 (3.6)     | 0.0 (0.0)   | 5.4 (0.1)  | 41.0 (9.3)     |
| CO (Tg yr <sup>-1</sup> )                               | 608.3 (67.3)                          | 459.1 (322.6)   | 159.3 (159.3) | 19.8 (19.8) | 1.2 (0.03) | 1247.7 (569.0) |
| C <sub>2</sub> H <sub>4</sub> (Tg C yr <sup>-1</sup> )  | 6.4 (1.1)                             | 5.4 (3.6)       | 4.3 (4.3)     | 1.2 (1.2)   | 0.2 (0.01) | 17.5 (10.2)    |
| C <sub>2</sub> H <sub>6</sub> (Tg C yr <sup>-1</sup> )  | 2.6 (0.5)                             | 2.5 (1.5)       | 0.8 (0.8)     | 0.8 (0.8)   | 0.12 (0.0) | 6.8 (3.5)      |
| C <sub>3</sub> H <sub>6</sub> (Tg C yr <sup>-1</sup> )  | 7.7 (1.0)                             | 4.7 (2.8)       | 0.9 (0.9)     | 1.3 (1.3)   | 0.3 (0.01) | 14.9 (6.0)     |
| C <sub>3</sub> H <sub>8</sub> (Tg C yr <sup>-1</sup> )  | 2.8 (0.2)                             | 1.6 (0.5)       | 1.6 (1.6)     | 1.0 (1.0)   | 0.4 (0.01) | 7.4 (3.4)      |
| CH <sub>2</sub> O (Tg yr <sup>-1</sup> )                | 3.2 (0.1)                             | 5.8 (4.0)       | 0.0 (0.0)     | 0.0 (0.0)   | 0.0 (0.0)  | 9.0 (4.1)      |
| Acetone (Tg yr <sup>-1</sup> )                          | 2.2 (0.0)                             | 2.9 (2.4)       | 24.3 (24.3)   | 0.0 (0.0)   | 0.0 (0.0)  | 29.4 (26.8)    |
| CH <sub>3</sub> OH (Tg yr <sup>-1</sup> )               | 0.8 (0.1)                             | 11.9 (7.6)      | 228.2 (228.2) | 0.0 (0.0)   | 0.0 (0.0)  | 240.9 (236.0)  |
| C <sub>2</sub> H <sub>5</sub> OH (Tg yr <sup>-1</sup> ) | 4.5 (0.6)                             | 0.1 (0.05)      | 9.2 (9.2)     | 0.0 (0.0)   | 0.0 (0.0)  | 13.8 (9.9)     |
| C <sub>4</sub> H <sub>10</sub> (Tg yr <sup>-1</sup> )   | 43.0 (0.6)                            | 0.9 (0.7)       | 0.0 (0.0)     | 0.0 (0.0)   | 1.2 (0.03) | 45.1 (1.3)     |
| Isoprene (Tg yr <sup>-1</sup> )                         | 0.0 (0.0)                             | 0.8 (0.3)       | 564.7 (564.7) | 0.0 (0.0)   | 0.0 (0.0)  | 565.5 (565.1)  |
| Terpenes (Tg yr <sup>-1</sup> )                         | 0.0 (0.0)                             | 0.4 (0.2)       | 143.2 (143.2) | 0.0 (0.0)   | 0.0 (0.0)  | 143.6 (153.5)  |
| H <sub>2</sub> (Tg yr <sup>-1</sup> )                   | 21.3 (2.2)                            | 9.6 (5.2)       | 3.0 (3.0)     | 3.0 (3.0)   | 0.0 (0.0)  | 36.9 (13.4)    |
| NH <sub>3</sub> (Tg yr <sup>-1</sup> ) <sup>a</sup>     | 37.5 (7.3)                            | 10.5 (6.1)      | 3.1 (3.1)     | 9.9 (9.9)   | 0.0 (0.0)  | 61.0 (26.5)    |
| SO <sub>2</sub> (Tg S yr <sup>-1</sup> )                | 46.4 (1.5)                            | 1.9 (1.2)       | 0.0 (0.0)     | 0.0 (0.0)   | 5.5 (0.1)  | 53.8 (2.8)     |
| BC (Tg C yr <sup>-1</sup> )                             | 5.0 (1.3)                             | 2.6 (2.0)       | 0.0 (0.0)     | 0.0 (0.0)   | 0.1 (0.0)  | 7.7 (3.3)      |
| OM (Tg C yr <sup>-1</sup> )                             | 29.7 <sup>b</sup> (18.0) <sup>b</sup> | 37.2 (28.8)     | 30.4 (30.4)   | 15.5 (15.4) | 0.2 (0.0)  | 113.0 (92.6)   |
| Aircraft NO (Tg N yr <sup>-1</sup> )                    |                                       |                 |               |             |            | 0.8 (0.0)      |
| Aircraft SO <sub>2</sub> (Tg yr <sup>-1</sup> )         |                                       |                 |               |             |            | 0.1 (0.0)      |
| Fuel use (Tg yr <sup>-1</sup> )                         |                                       |                 |               |             |            | 122.0 (0.0)    |
| Dust (Tg yr <sup>-1</sup> )                             |                                       |                 |               |             |            | 1221 (1237)    |
| Sea Salt (Tg yr <sup>-1</sup> )                         |                                       |                 |               |             |            | 6188 (6324)    |
| Dimethyl sulfide (Tg yr <sup>-1</sup> )                 |                                       |                 |               |             |            | 36.2 (36.0)    |

<sup>a</sup> Emissions of NH<sub>3</sub> also include 0.1 Tg yr<sup>-1</sup> from animals.

<sup>b</sup> Includes 9.6 Tg C yr<sup>-1</sup> as secondary organic aerosol from the oxidation of anthropogenic NMVOC calculated using offline butane emissions and OH concentrations.

Table 3. Annual mean global budget and burdens simulated by AM3. Average values and interannual standard deviations over the baseline 1981-2000 time period are shown in column 2. Effect of changing short-lived pollutant emissions from 1860 to 2000 levels on global budget and burdens are shown in column 3 as absolute differences (2000-1860) and percent differences in parentheses.

|  | Annual average (1981-2000) $\pm$ Standard Deviation | 2000 – 1860                  |
|--|---|------------------------------|
| <b>Tropospheric Ozone Budget</b>                             |   |                              |
| Photochemical Production (Tg yr <sup>-1</sup> )              | 5753 $\pm$ 244                                      | 1815 (45%)                   |
| Photochemical Loss (Tg yr <sup>-1</sup> )                    | 5092 $\pm$ 203                                      | 1452 (40%)                   |
| Net Photochemistry (Tg yr <sup>-1</sup> )                    | 661 $\pm$ 46  | 363 (79%)                    |
| Dry Deposition (Tg yr <sup>-1</sup> )                        | 1205 $\pm$ 20                                       | 404 (48%)                    |
| Cross-tropopause flux (Tg yr <sup>-1</sup> )                 | 443 $\pm$ 27  | 34 (9%)                      |
| Ozone Burden (Tg)  | 360 $\pm$ 7   | 64 (21%)                     |
| Global Total Column Ozone (DU)                               | 303 $\pm$ 5   | 9.1 (3%)                     |
| Tropospheric OH Concentration (molec cm <sup>-3</sup> )      | 1.05 $\pm$ 0.02x10 <sup>6</sup>                     | 0.09 x 10 <sup>6</sup> (10%) |
| Tropospheric Methane Lifetime (yr)                           | 8.5 $\pm$ 0.2                                       | -1.5 (-14%)                  |
| Lightning NO <sub>x</sub> Emissions (Tg N yr <sup>-1</sup> ) | 4.5 $\pm$ 0.2                                       | -0.3 (-6.4%)                 |
| <b>Global Total Burdens</b>                                  |   |                              |
| Carbon Monoxide (Tg)   | 335 $\pm$ 11  | 82 (30%)                     |
| Tropospheric NO <sub>x</sub> (Gg N)                          | 195 $\pm$ 6.3                                       | 45 (30%)                     |
| Black Carbon (Gg C)  | 126 $\pm$ 6.5                                       | 76 (140%)                    |
| Sulfate (Gg S)   | 572 $\pm$ 16.5                                      | 369 (207%)                   |
| Organic Carbon (Gg C)  | 1776 $\pm$ 66                                       | 503 (40%)                    |

## Figures

Figure 1. Change in annual mean surface emissions in percent from 1860 to 2000 levels for nitrogen oxide (NO), carbon monoxide (CO), non-methane volatile organic compounds (NMVOCs), black carbon (BC), organic carbon (OC), and sulfur dioxide (SO<sub>2</sub>). Surface emissions include emissions from anthropogenic sources, biomass burning, and ships.

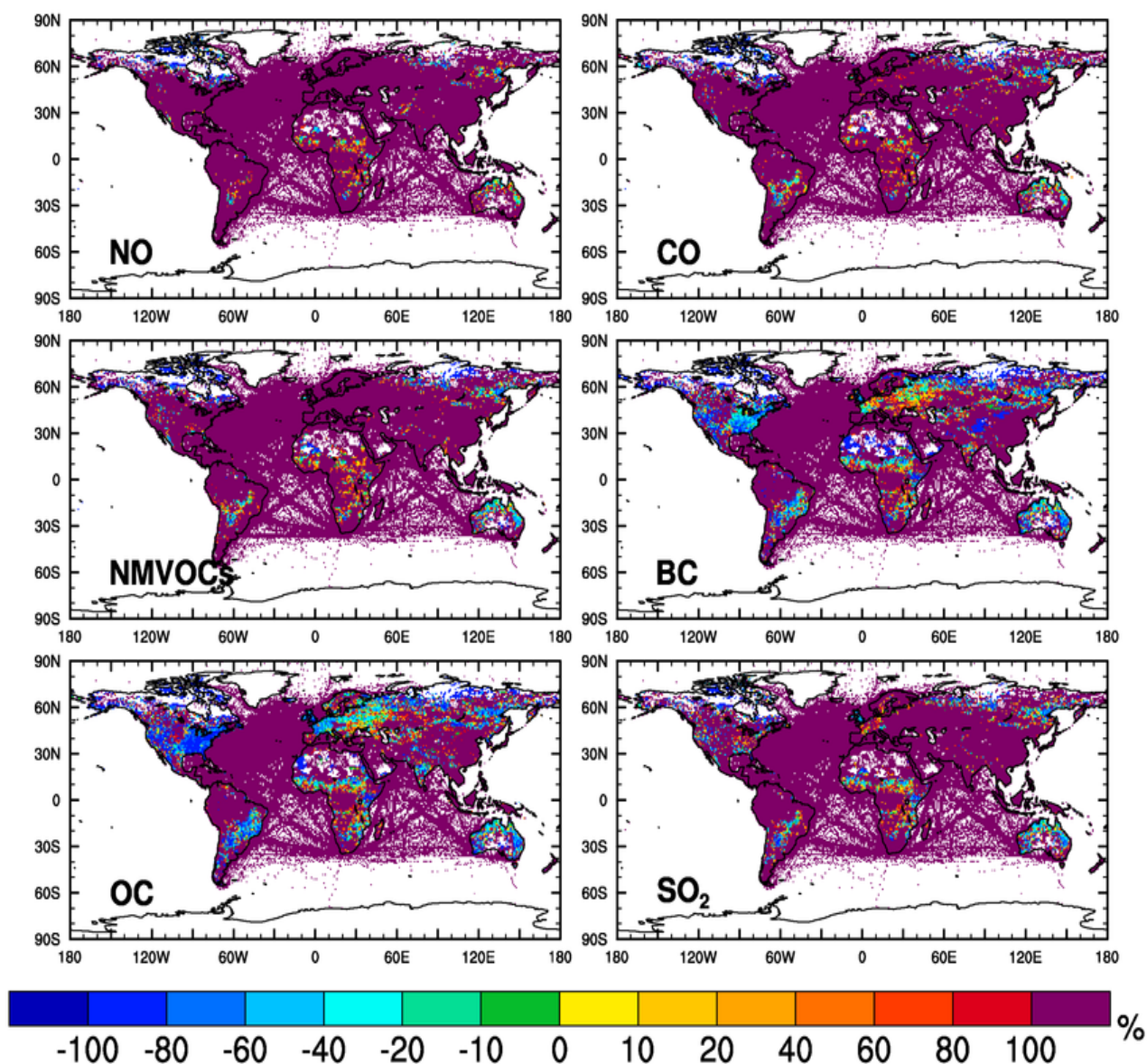


Figure 2. Comparison of simulated monthly mean ozone (ppbv) with observed ozonesonde climatology for the period 1995 and 2009 at vertical levels of 800 (left), 500 (center) and 200 hPa (right). Model ozone is averaged for 1981-2000 (red) and 1995-2007 (blue) time periods. Monthly mean observations are shown in black dots and the median are in blue dots. Vertical lines are the standard deviations.

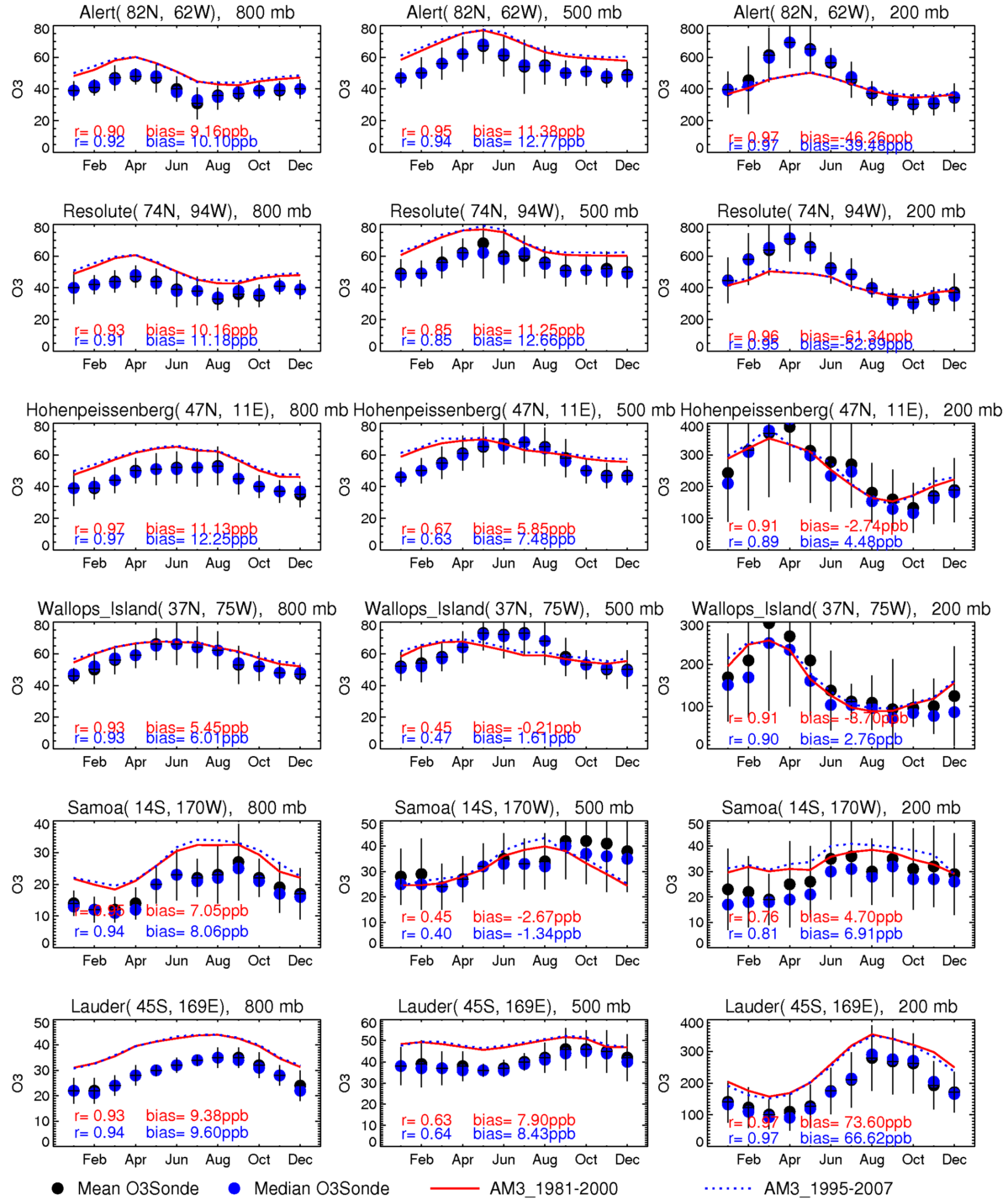


Figure 3. Zonal annual mean absolute bias of AM3 a)  $O_3$  and b) CO concentration relative to measurements by the Tropospheric Emission Spectrometer (TES) aboard the Aura satellite for the period 2005 to 2007. Bias is calculated as AM3 minus TES in units of ppbv.

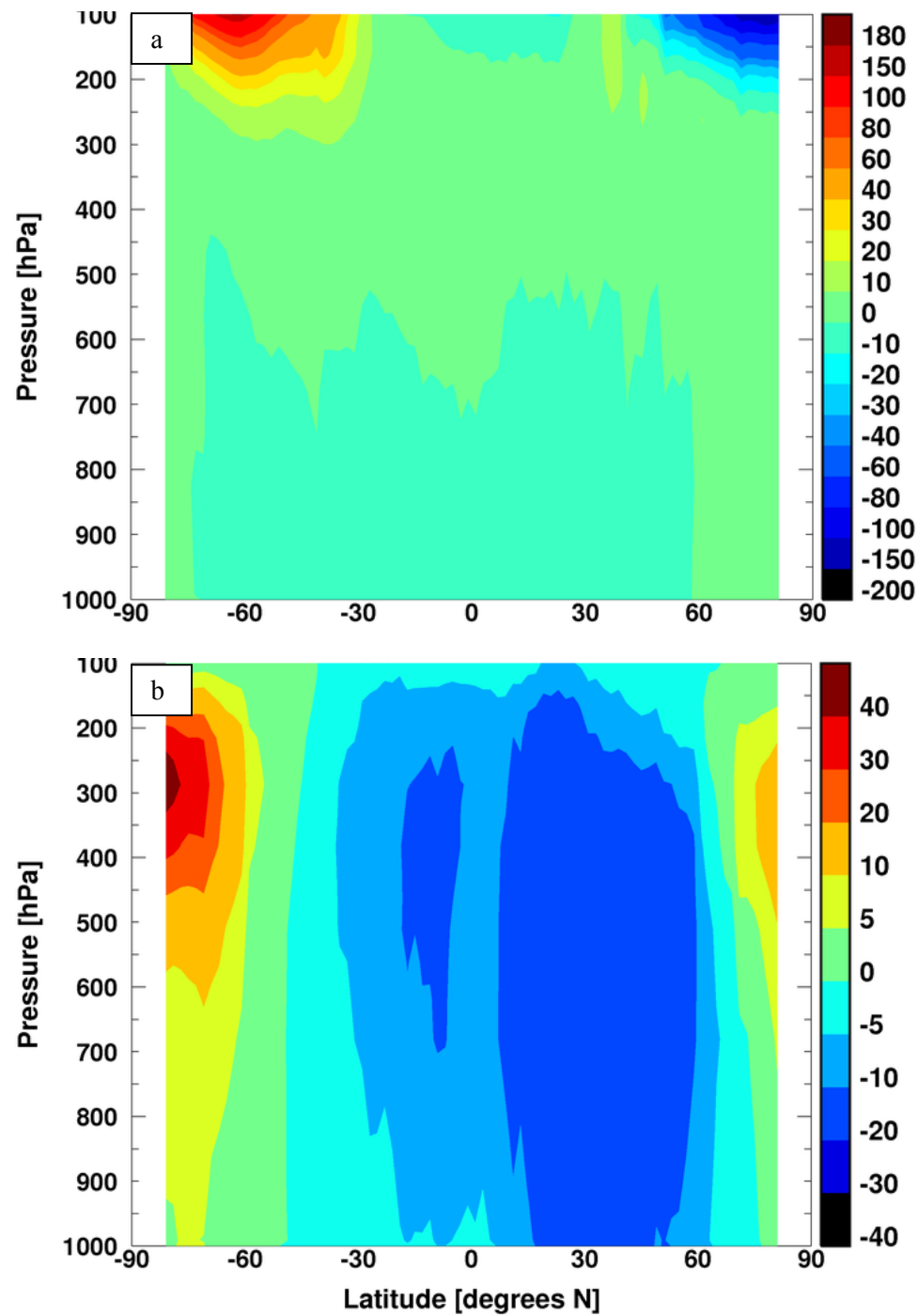


Figure 4. Comparison of model simulated monthly mean (red line) with observed CO concentrations (black dots) at surface sites. Observations are from Novelli and Masarie (2010) for the 1988 to 2010. Vertical lines represent the standard deviations of the observations within a month.

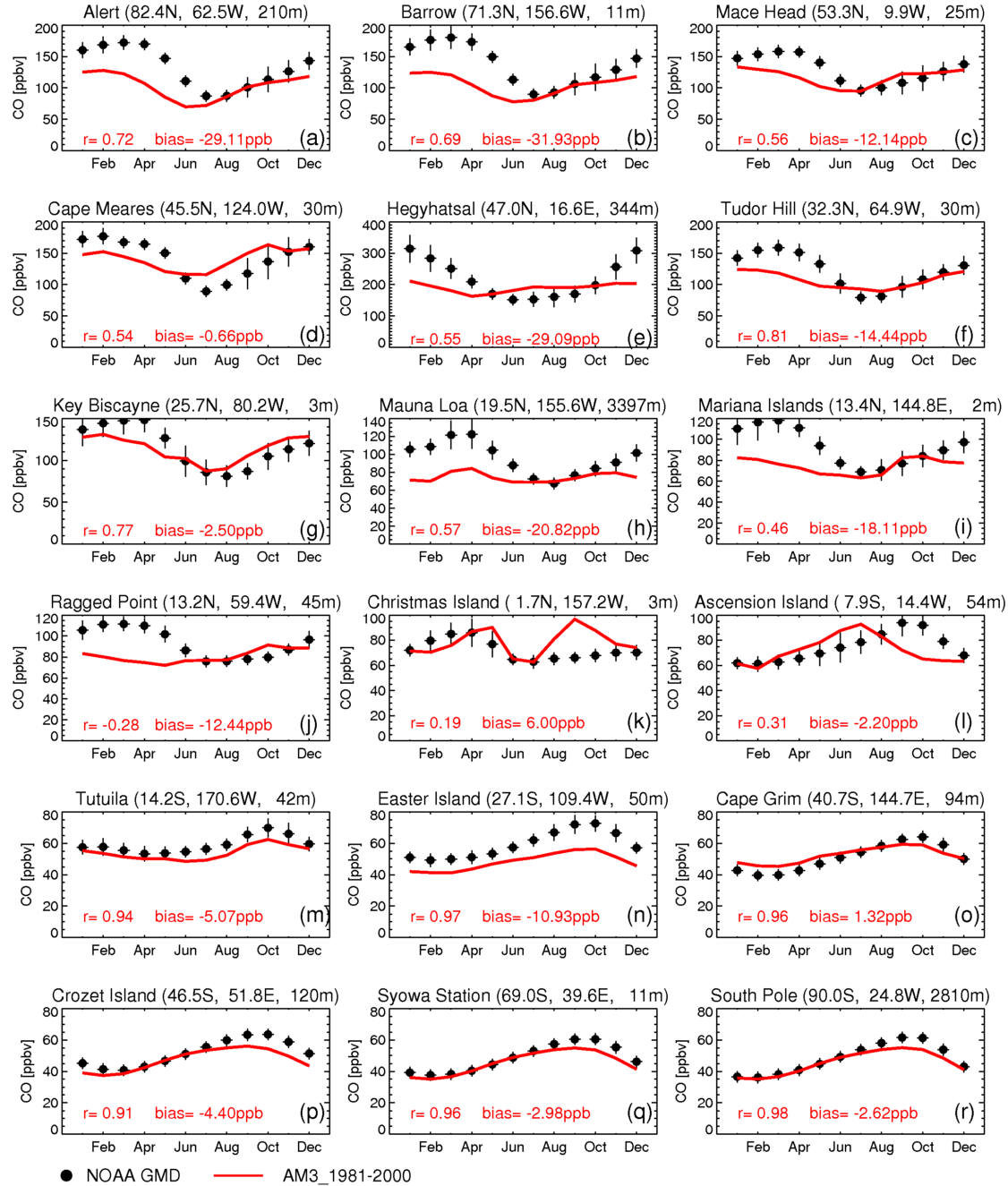


Figure 5. (a) Annual mean OH burden from AM3 compared with the (b) climatological mean of Spivakovsky et al. [2000], (c) percent change in airmass-weighted mean OH concentrations in various subdomains of the atmosphere and (d) ratio of present-day (2000) to preindustrial (1860) mean OH in the surface to 750 hPa subdomain of the atmosphere.

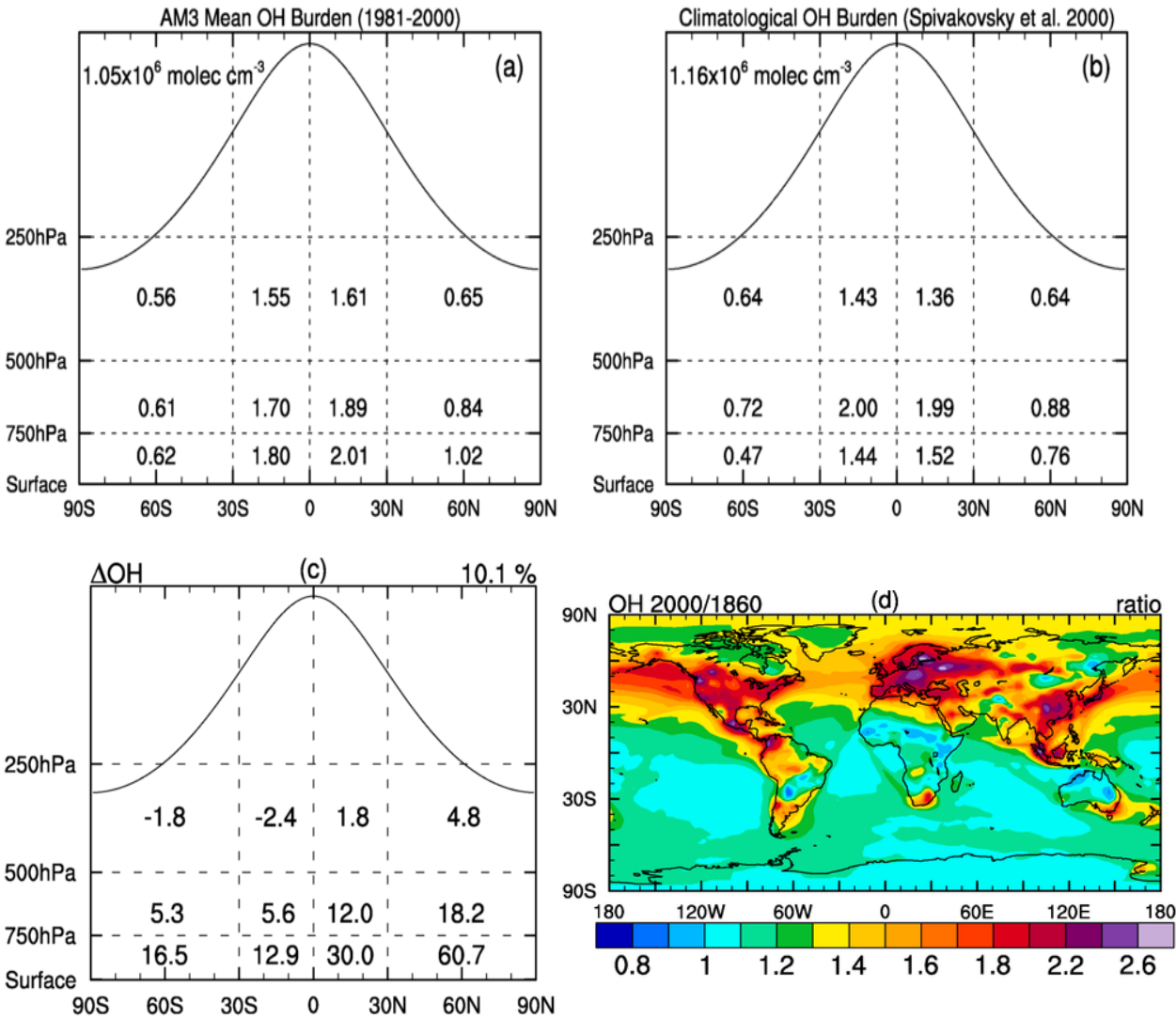


Figure 6. AM3 simulated changes in column burden (left panel) and surface (right panel) concentrations of a, b)  $O_3$  (DU, ppbv), c, d)  $CO$  (Tg, ppbv), e, f) tropospheric  $NO_x$ , g, h) sulfate ( $SO_4^-$ ), i, j) black carbon (BC), and l, k) organic carbon (OC) in response to short-lived pollutant emission changes from preindustrial to present day (2000-1860). Areas where change is insignificant ( $p=95\%$  student's t-test) are not colored.

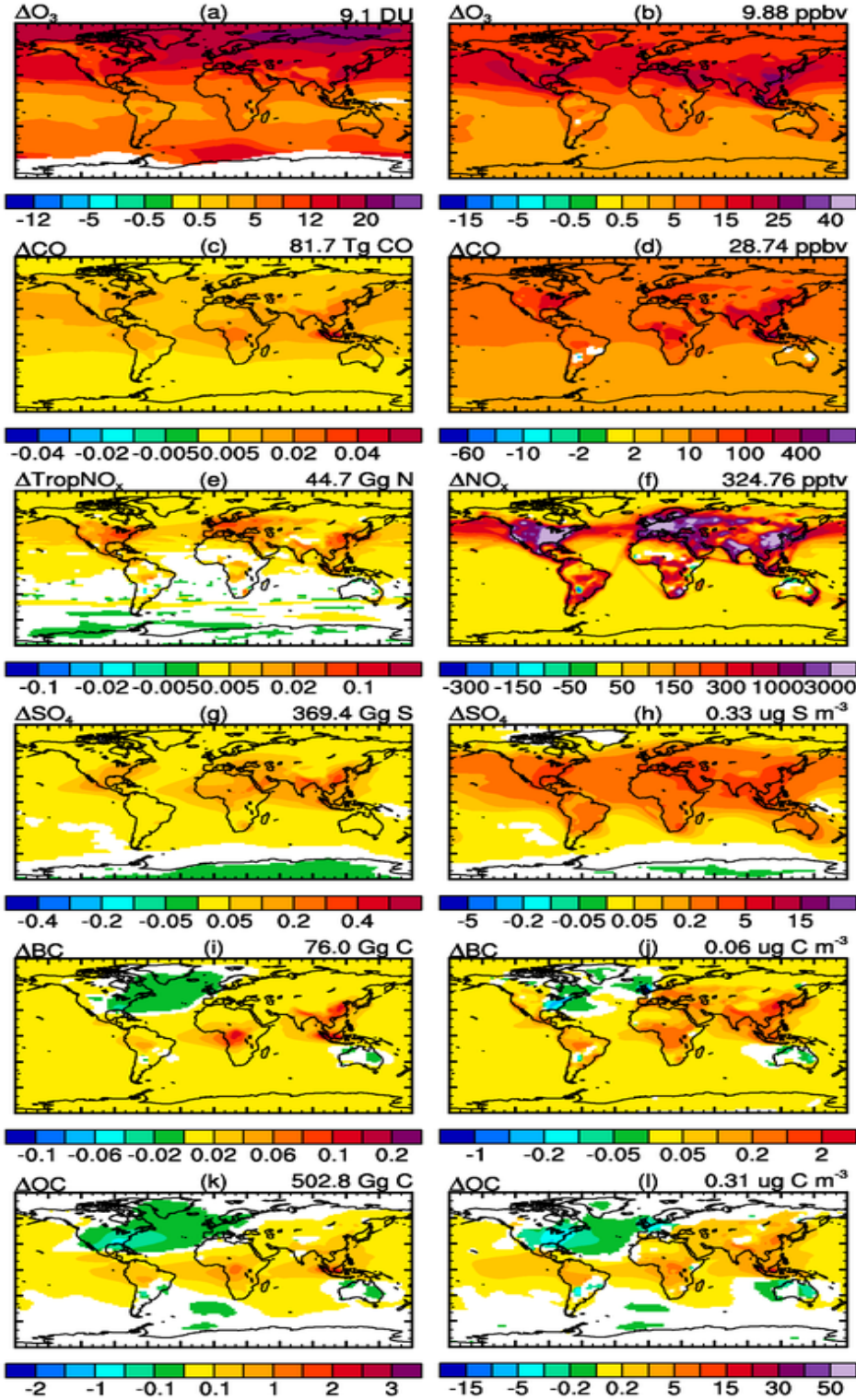


Figure 7. Net annual mean top-of-the-atmosphere a) all-sky radiative perturbation flux (RFP), b) clear-sky RFP, and c) cloudy-sky RFP, due to changes in short-lived pollutant emissions from preindustrial to present-day. Global mean values are indicated at top right of each plot. Areas where change is insignificant ( $p=95\%$  student's t-test) are not colored.

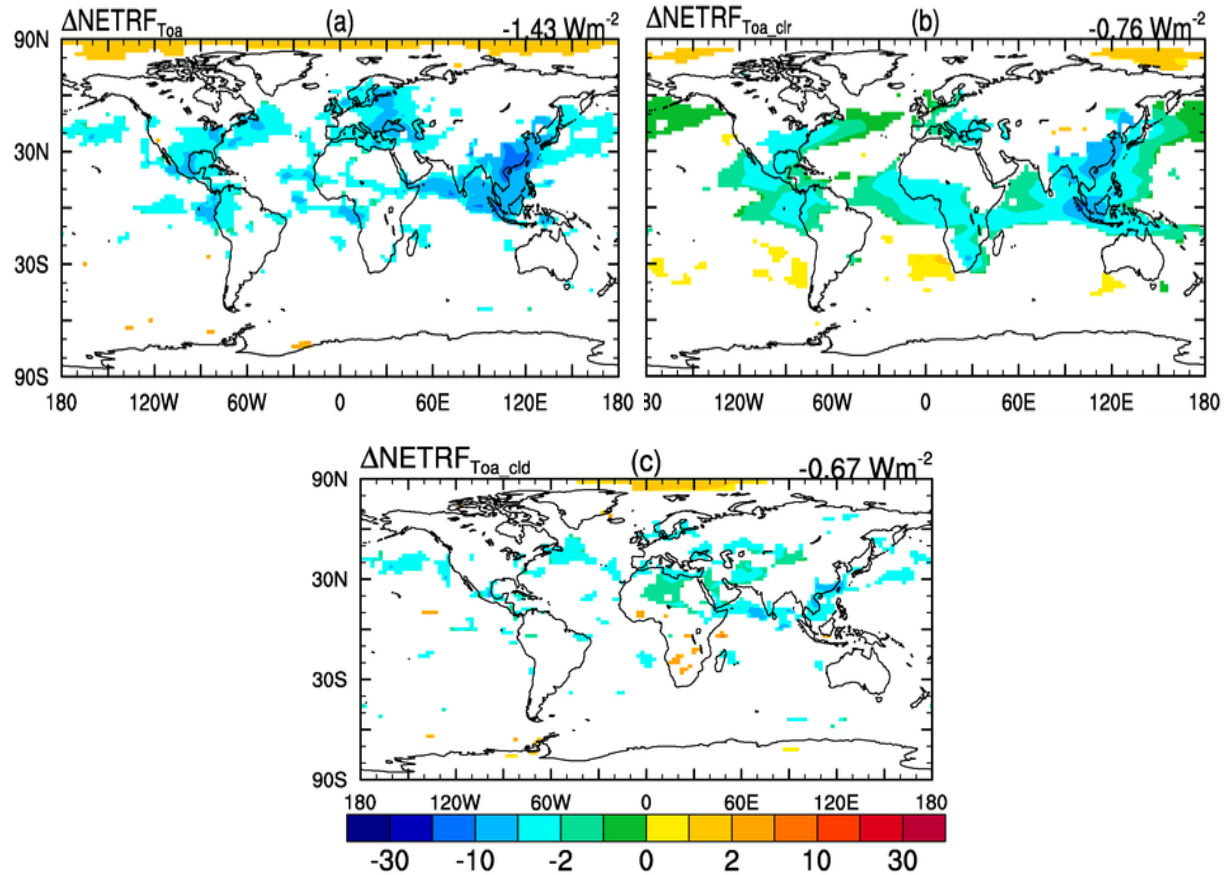


Figure 8. Net annual mean surface a) all-sky radiative perturbation flux (RFP), b) clear-sky RFP, and c) cloudy-sky RFP, due to changes in short-lived pollutant emissions from preindustrial to present-day. Global mean values are indicated at top right of each plot. Areas where change is insignificant ( $p=95\%$  student's  $t$ -test) are not colored.

